Twinning effects in the single/nanocrystalline cubic silicon carbide subjected to nanoindentation loading

Saeed Zare Chavoshi[1*], Shuozhi Xu[2]

[1]Department of Mechanical Engineering, Imperial College London, London SW7 2AZ, UK

[2]California NanoSystems Institute, University of California, Santa Barbara, Santa Barbara, CA 93106-6105, USA

*Corresponding author: *s.zare@imperial.ac.uk*

Abstract

Certain nanotwinned metals exhibit superior properties originating from the coherent internal interfaces; however, the deformation mechanisms responsible for strengthening/softening behaviour in nanotwinned ceramics with covalent bonds are less clear. Here we carry out parametric atomistic simulations to provide insight into underlying deformations physics and responses of nanotwinned single/nanocrystalline cubic silicon carbide subjected to nanoindentation loading. Our simulations predict superior nanocontact resistance of nanotwinned single crystals, originating from the lattice dislocation blockage effects of coherent twin boundaries (CTBs), with a clear dependence on the CTB density. Nanotwinned nanocrystals exhibit an inverse Hall-Petch-like effect when the average grain size is larger than 8 nm, whereas fine grain size nanotwinned nanocrystals show slightly improved indentation hardness compared to their twin-free counterparts. We unravel that regardless of the CTB spacing, grain boundaries, lattice dislocation glide, and CTBs collectively accommodate the imposed plastic strain by the indenter in the nanocrystalline substrates with large grain sizes; however, with a decreasing grain size, the contributions by lattice dislocations and CTBs becomes limited. Our results also show that lattice dislocation-CTB interactions and

transmission mechanisms, i.e. nucleation of twinning partial dislocations and formation and annihilation of point defects at CTBs, are insensitive to test conditions such as temperature, indentation speed, and indenter size. However, with decreasing CTB spacing, twinning dislocation occurs via dissociation and propagation of mostly Shockley partials rather than Frank partials trapped at CTBs. The structure-property findings in this study render unique insights to design novel nanotwinned silicon carbide nanostructures with improved indentation mechanical properties and high plasticity.

Keywords: Twinning; Grain boundary; Nanoindentation; Molecular dynamics; Silicon carbide

1. Introduction

Nanotwinned metallic materials have attracted considerable interest over the last decade following the discovery of their much higher hardness and strengths compared with their twin-free counterparts [1]. In fact, strengthening polycrystalline metals by reducing the grain size, known as the Hall-Petch effect [2, 3], originates from the smaller length of the dislocation pile-up and so the lower internal stress exerted on the leading dislocation in front of grain boundaries (GBs) [4, 5]. For twin boundaries (TBs), the twin thickness also exhibits a "Hall-Petch-like" effect in that the maximum strength of the nanotwinned nanocrystal is reached at 2 nm [6] or 15 nm [7]. TBs, however, might lower the yield strength of some metals, e.g., Pd [8] and W [9-11] as they can provide nucleation sites for dislocations or migrate during the deformation process.

While interactions amongst dislocations, TBs, and GBs are known to be the underlying mechanism of simultaneous high strength and high ductility in certain nanotwinned metals [12], the strengthening/softening mechanisms in nanotwinned ceramics are less clear since dislocation activities are less pronounced in ceramics owing to their strong covalent or ionic bonding [13]. Indeed, there is scarcity of research on the nanotwinned ceramic materials subjected to various forms of loadings. Recent experiments reported that synthetic nanotwinned diamond with an average twin thickness of 5 nm exhibits ultra-high Vickers hardness and fracture toughness up to 200 GPa and 14.8 MPa $m^{1/2}$, respectively [14]. It is believed that the presence of ultrafine nanotwins introduces extra hardening to diamond, which is probably due to both the Hall-Petch and quantum confinement effects at the nanoscale, while gliding of dislocations along densely distributed TBs enhances fracture toughness of diamond [14]. Under indentation loading, molecular dynamics (MD) studies have revealed that the conventional Hall-Petch strengthening due to TBs blocking dislocation motion may result in the hardening of the diamond, while the softening could be attributed to the formation and

movement of the dislocation loops parallel with the surface and the breakage of TBs, which may serve as new sites for dislocations nucleation [15].

Nanotwinned cubic boron-nitride (cBN) ceramic with a twin thickness down to 3.8 nm has shown a superior combination of extremely high Vickers hardness (exceeding 100 GPa) and large fracture toughness (> 12 MPa $m^{1/2}$) [16]. *Ab initio* density functional theory (DFT) calculations reveal that such a high hardness of nanotwinned cBN might be related to the high energy barrier for Shockley partials, which may dominate plastic deformation in cBN [17]. DFT simulations show that the theoretical shear strength of boron carbide (B_4C) hard ceramic can be exceeded by 11% by imposing nanoscale twins. In addition, the indentation strength of nanotwinned B_4C is found 12% higher than that of the perfect crystal which is attributed to the suppression of TB slip within the nanotwins due to the directional nature of covalent bonds at the TB [18, 19]. DFT studies also demonstrate that the intrinsic shear strength of single crystalline boron-rich boron carbide ($B_{13}C_2$) is higher than that of single crystalline B_4C. But nanotwins in $B_{13}C_2$ lower the shear strength, making it softer than single crystalline B_4C. This reduction in strength of nanotwinned $B_{13}C_2$ arises from the interaction of the TB with the C-B-C chains that connect the B_{12} icosahedra [20]. Moreover, DFT supported by transmission electron microscopy (TEM) suggests that amorphous bands nucleate preferentially at the TBs in boron-suboxide (B_6O) ceramic since the twinned structure has a maximum shear strength of 7.5% lower than that of its twin-free counterpart. It is also found that, under pure shear deformation, the slip system with the lowest resolved shear stress is (010)/⟨001⟩ which transforms τ-B_6O to R-B_6O. Nonetheless, under indentation conditions, the lowest stress slip system alters to (001)/⟨110⟩, culminating in icosahedra disintegration and hence amorphous band formation [21, 22].

As a wide (tunable)-band gap semiconductor, silicon carbide (SiC) is a very promising ceramic for potential applications in nuclear energy systems and microelectronics due to its excellent

properties of high radiation tolerance, high strength, high thermal conductivity, high chemical stability, high resistance to shock, low thermal expansion, low density, high refractive index, and chemical inertness [23]. Accordingly, SiC is believed to be a potential replacement to leading horse material Si [24-27] on many applications including micro-/nanoelectromechanical systems (MEMS/NEMS). SiC exhibits one-dimensional polymorphism characterized by different stacking sequences of the Si-C bilayers. The cubic silicon carbide (3C-SiC), as a zinc blende structured SiC, possesses the highest fracture toughness, hardness, electron mobility, and electron saturation velocity amongst all SiC polytypes [28]. Compressibility experiments of synthetic periodically twinned 3C-SiC nanowires show that the bulk modulus can be increased up to 316 GPa, which is 20-40% higher than 3C-SiC of other morphologies including micron and nanosized particles, as well as twin-free nanowires [29, 30]. MD simulations demonstrate that the critical strain to yielding of the (111)-oriented 3C-SiC nanowires can be enhanced by twinning, and the critical stress (yield stress) increases with decreasing TB spacing. However, the critical stress of the twinned nanowires is found to be lower than those of the twin-free counterparts [31]. Nanoscale wear studies of nanocrystalline 3C-SiC using MD show that the GB sliding is the primary deformation mechanism, which lowers the scratch hardness relative to the single crystal [32]. It is also suggested that the two-phase character, i.e. crystalline and disordered, of nanocrystalline ceramics including 3C-SiC can lead to unusual indentation-induced deformation mechanisms, in which an interplay and competition between crystalline intragranular and disordered intergranular responses take place [33]. A few other MD simulation studies of thermal transport [34, 35] and radiation effects [36-41] in 3C-SiC substrates encompassing either TBs or GBs have also been reported in the literature.

In spite of the aforementioned studies of 3C-SiC ceramic, the role of nanoscale twins in deformation mechanisms of the single/nanocrystalline 3C-SiC in nanoscale contact mechanics

problems have not been as rigorously examined. 3C-SiC MEMS/NEMS [42] are often subjected to localized contact loading of surface atoms. Of the wide variety of characterisation techniques, nanoindentation is one of the most rigorous approach to gaining information about local material properties, as well as fundamental deformation mechanisms [43, 44]. In this context, MD simulation of nanoindentation can provide insights by allowing monitoring of nanomechanical response, defect nucleation, and internal microstructure evolution of the material subjected to mechanical loading. Herein we employ MD simulation to delve into how TBs affect the nanoindentation deformation properties of nanotwinned single/nanocrystalline 3C-SiC ceramic, and to unveil whether/how Hall-Petch effect is exhibited by strengthening/softening of nanotwinned 3C-SiC under nanoindentation loading. The influences of the indenter size, temperature, and indentation speed on the plasticity of twinned 3C-SiC will also be explored. It is envisioned that the structure-property relationships obtained in this work can set a framework for design and fabrication of nanostructured 3C-SiC samples with enhanced indentation mechanical properties.

2. Methods

2.1. Crystallographic structure of twins

Understanding the crystallographic structure of TBs at the atomic scale is indispensable so as to appropriately tailor twins to attain a proper twin structure and desired properties. Diamond cubic 3C-SiC lattice comprises two interpenetrating face-centered cubic (fcc) lattices, thus, the $\sum 3$ coherent TBs (CTBs) in nanotwinned 3C-SiC lie on {111} planes, similar to those in fcc metals. According to the lattice structure of 3C-SiC, three crystallographic structure of twins can be assumed: I) symmetric Si-Si bonded twin with complete mirror lattices on both sides of the TB (Figure 1a), II) symmetric C-C bonded twin with complete mirror lattices on both sides

of the TB (Figure 1b), III) asymmetric Si-C bonded twin without mirror symmetry (Figure 1c). In order to determine the most energetically stable twin structure of 3C-SiC, we calculate the CTB energy of these three $\sum 3$ CTBs and select the one which offers the lowest energy. The CTB energy can be obtained by finding the difference between two total energies: the total energy of the supercell containing CTB (E_{twin}), and the total energy of the supercell without CTB (E), as given in Eq. (1)

$$E_{\mathrm{TB}} = (E_{\mathrm{twin}} - E)/A_{\mathrm{twin}} \quad (1)$$

where A_{twin} denotes the area of CTB. Values of E_{TB} and E are calculated using an open source computer code LAMMPS [45]. Two supercells containing 90,240 atoms respectively — one with a CTB parallel to the *X*-*Z* plane and another twin-free — are built, with periodic boundary conditions (PBCs) applied along the *X* and *Z* directions. The calculated CTB energies, E_{TB}, after energy minimization for diamond 3C-SiC, modelled by the Vashishta interatomic potential function [46], are summarized in Table 1, where the asymmetric twin without mirror symmetry (Figure 1c) exhibits the lowest CTB energy. Hence, we pursue our MD simulations of nanotwinned single/nanocrystalline 3C-SiC using this CTB system. Notice that such CTB system is experimentally achievable [29, 30].

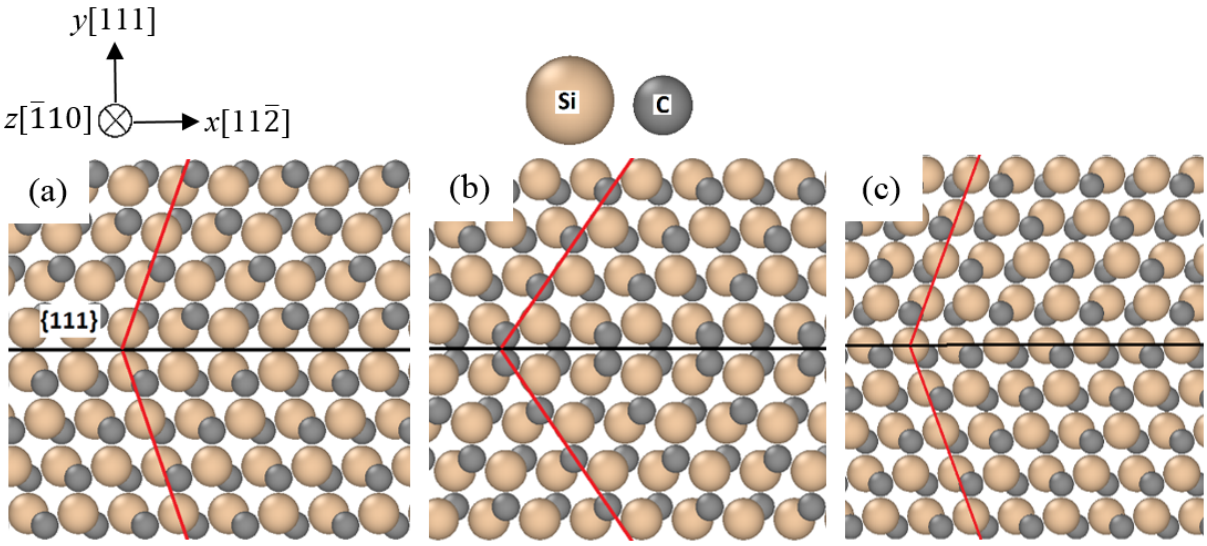

Figure 1 Schematic illustrations of atomic arrangements of {111} ∑3 CTBs in 3C-SiC: (a) Symmetric Si-Si bonded twin with complete mirror lattices on both sides of the CTB; (b) Symmetric C-C bonded twin with complete mirror lattices on both sides of the CTB; (c) Asymmetric Si-C bonded twin without mirror symmetry.

Table 1 Calculated CTB energy for diamond 3C-SiC.

Twin system	**CTB energy (J/m^2)**
Symmetric Si-Si bonded twin with complete mirror lattices on both sides of the CTB (Figure 1a)	5.0
Symmetric C-C bonded twin with complete mirror lattices on both sides of the CTB (Figure 1b)	8.284
Asymmetric Si-C bonded twin without mirror symmetry (Figure 1c)	0.114

2.2. Surface energies

Surface energy is another important property to test since it can affect crack or dislocation nucleation from surface. The surface energy (E_s) calculation is similar to the CTB energy calculation, i.e.

$$E_s = (E_{sb} - E)/A \quad (2)$$

where E_{sb} and A, respectively, are the energy of the surface block and the surface area. Table 2 demonstrates the relaxed surface energies of the (111) plane, signifying that while Si atoms are on the surface, the system has low surface energy. According to these results, we select the 3C-SiC substrates with Si atoms on the surface for the nanoindentation studies in this work. In fact, our simulations showed that while C atoms are on the surface, the substrate starts to explode when the indenter is approaching (but not in contact).

Table 2 Surface energy of the (111) plane for diamond 3C-SiC.

Surface system	**Surface energy (J/m^2)**
Si atoms on the surface	2.27
C atoms on the surface	15.59

2.3. Details of the MD simulation

Atomic-scale computer simulations of materials such as MD rely on a prescription of the energy in terms of the atomic positions, which is often referred to as the interatomic potential. Since the validity of MD simulation results very much depends on the interatomic potential, precautions are required when selecting potential function for a specific system and process [5, 9, 47-49]. In this study, the Vashishta interatomic potential function [46], which makes use of a modified function of the Stillinger-Weber model [50] for the three-body term, is adopted to dictate the interactions between atoms within the 3C-SiC substrate as this interatomic potential well reproduces the generalized stacking fault energies, cohesive energy, elastic constants, and melting point of 3C-SiC [46].

The geometrical details and process parameters are given in Table 3. The atomic structure of the simulated single crystal substrate is aligned with $[11\bar{2}]$, $[111]$, and $[\bar{1}10]$ orientations along the *X*, *Y*, and *Z* directions, respectively. The initial nanocrystalline structure is generated from a Voronoi tessellated structure. Atoms of the substrate are divided into two zones, namely boundary atoms and Newton atoms. The boundary atoms at the bottom of the substrate normal to the *Y* direction are held rigid to prevent the substrate from shifting whereas the atoms in the Newton region follow isothermal-isobaric (NPT) dynamics at zero pressure. PBCs are imposed in both *X* and *Z* directions to reduce the effects of the simulation cell size. Velocity Verlet algorithm with a time step of 1.0 fs is employed for the time integration of Newton's equations of motion.

Table 3 Details of the MD simulation models and the nanoindentation parameters. The asymmetric twin without mirror symmetry shown in Figure 1c is used. λ and *d* represent the CTB spacing and mean grain size, respectively.

Material systems	Single crystal 3C-SiC	λ: 1.5, 3, 6, 8, 12 nm
	Nanocrystalline 3C-SiC	*d*: 4, 8, 15 nm λ: 1.5, 3, 6, 8, 12 nm; λ<*d*
Interatomic potential function	Vashishta potential [46]	
Ensemble	NPT	
Time step	1.0 fs	
Boundary conditions	Periodic in the *X* and *Z* directions, while the boundaries normal to the *Y* direction are traction-free	

Dimension of the substrate	~ 25×25×25 nm^3
Number of atoms in the substrate	~ 1.5 millions
Radius of spherical indenter	4, 6, 8 nm
Indentation speed	5, 10, 50, 100 m/s
Temperature	10, 300, 600, 1000, 2000 K

The substrate is indented by a rigid spherical indenter, and the maximum indentation depth is equal to the indenter radius. If the ratio of the indentation depth to the indenter radius is too large, the indented surface shows pile-up effects [51]. Note that the Berkovich tip with rounded tip radius of up to 50 nm is normally employed in nanoindentation studies; therefore, it is sensible to expect that the spherical indenter utilized in this study can produce the analogous plastic deformation generated by a Berkovich tip prior to substantial influences produced by the pyramidal planes [52]. The interaction between the indenter and the substrate is assumed to be purely repulsive. The repulsive force $F(r)$ is given by $F(r) = -K(r - R)^2$, where K is the indenter stiffness, r is the distance between the atom to the center of the indenter, and R is the indenter radius [53]. In this study, stiffness K is set to $10\ \mathrm{eV/A^3}$ [54, 55]. The indentation process is performed in a displacement controlled mode by applying a constant speed to the indenter perpendicularly toward the substrate [53]. At the beginning of a simulation, the indenter is set at a distance of 0.5 nm above from the substrate. To relax the randomly introduced GBs before performing nanoindentation simulations, all pairs of atoms at the GBs whose distance of separation is smaller than 0.9 Å are searched for and one of the two atoms is removed, so that the abnormally high atomic density regions at the GBs are eliminated which

aids in minimizing the system energy [56]. Then, energy minimization is carried out using a conjugate gradient algorithm followed by a dynamic relaxation through 30,000 MD time steps under NPT ensemble to reach the thermal equilibrium state at the target temperature. Simulation results are visualized and analyzed using OVITO [57], an open source software in which dislocations are identified by the dislocation extraction algorithm (DXA) [58]. The DXA algorithm is based on a discrete Burgers circuit integral over the elastic displacement field and is not limited to specific lattices or dislocation types [27]. The indentation hardness, H, can be evaluated by the load-displacement curve, and it is defined as the ratio of load (P) to the projected contact area S, i.e. $H = P/S$, where $S = \pi(2R - h_c)h_c$, with h_c being the contact depth. Extraction of accurate contact depth is difficult in MD studies, thus the projected contact area is usually calculated with $S = \pi(2R - h)h$ in plastic deformation region, where h is the indentation depth [59].

3. Results and discussion

3.1. Defect formation in nanotwinned single crystal 3C-SiC

Intense strain gradients and complex stress fields are imposed to the substrate by the indenter, leading to formation of a complicated defect network. Figure 2 renders the defect structure at h=6 nm, where numerous lattice dislocations are emitted and propagate in the 3C-SiC substrate, with CTBs blocking the dislocation migration within the samples through dislocation-CTB interactions. A key observation in Figure 2 is that in spite of high stress levels and resultant defect formation, the CTBs preserve their integrity. In other words, even closely spaced twins do not annihilate and reform, e.g., the so-called "detwinning" does not occur, signifying the nanotwin stability in 3C-SiC under nanoindentation loading. This observation is in contrast to nanotwinned nanopillars in body-centered cubic (bcc) W with λ=1 nm, where detwinning,

exhibited by annihilation of {112} twin layers as a result of partial dislocations gliding on CTBs, transpired under uniaxial tension and compression loading [11]. Instead, in the current study, destruction of nanoscale twins under nanoindentation loading is observed due to collision of indenter with CTBs.

In the following, we first discuss the defect-mediated plasticity in twin-free single crystal, then elaborate the deformation behavior and lattice dislocation-CTB interaction mechanisms in nanotwinned single crystals. The majority of this research work focuses on analysis of the deformation observed at the temperature (T) of 300 K and indentation speed of 50 m/s using an indenter with R=6 nm, with Section 3.3 dedicated to perceiving differences obtained by varying the temperature, indentation speed, and indenter radius.

Twin-free single crystal. Defect formation initiates with the formation of point defects at h~1.3 nm, followed by the nucleation of perfect dislocations forming a loop with Burgers vector of $\boldsymbol{b} = \frac{1}{2}[10\bar{1}]$ gliding on the $\{111\}$ planes (see Supplementary Movie 1). Note when the compatibility strains cannot be relaxed by heterogeneous dislocation nucleation, point defects are first formed beneath the indentation pit. U-shaped half loops $\boldsymbol{b} = \frac{1}{2} < 110 >$ with dislocation lines starting and terminating around the indentation region are generated and expanded at deeper penetration of the indenter yet they remain pinned to their nucleation sites. As shown in Figure 3, the first prismatic loop composed of perfect dislocations with $\boldsymbol{b} = \frac{1}{2}[\bar{1}\bar{1}0]$ direction perpendicular to the plane of the loop is emitted at h~1.8 nm, which is a result of "Lasso"-like mechanism i.e. glide of the edge component of shear loop, owing to the indentation stress field, away from the indentation pit while intersection and spontaneous pinching off of screw components. The observed "Lasso"-like mechanism is different from that found by Sun *et al.* [60], where the "Lasso"-like mechanism in 3C-SiC occurred via cross-slip of screw components. In fact, the "Lasso"-like mechanism via cross-slip has also been

observed in wurtzite structure AlN and GaN [61], bcc tantalum [52], and hexagonal close-packed (hcp) Mg, Ti, and Zr [62] subjected to indentation loading. Nucleation of perfect dislocations and the "Lasso"-like mechanism via intersection and annihilation of screw components continues to take place during further indentation, leading to the emission of other prismatic loops with $\boldsymbol{b} = \frac{1}{2}[1\bar{1}0]$ and $\boldsymbol{b} = \frac{1}{2}[\bar{1}01]$. The loops move away from the nucleation sites into the substrate interior owing to the far field stress induced by the indenter. The prismatic loops generated in the substrate are ~17-25 nm long at the stage of pinching off. Intrinsic stacking faults (ISFs) at the sides of the indentation region pinned to the surface formed by Shockley partials $\boldsymbol{b} = \frac{1}{6}[\bar{2}11]$ and $\boldsymbol{b} = \frac{1}{6}[\bar{1}\bar{1}2]$ appear and grow at h~2.2 nm. These ISFs are dragged towards the substrate interior and the associated Shockley partials react with other perfect dislocations forming junction-like dislocation structure. Also observed is dissociation of perfect dislocations $\boldsymbol{b} = \frac{1}{2}[\bar{1}10]$, forming U-shaped half loops attached to the surface, to Shockley partials $\boldsymbol{b} = \frac{1}{6}[\bar{1}21]$ and $\boldsymbol{b} = \frac{1}{6}[\bar{2}1\bar{1}]$, generating an ISF. As the indentation proceeds, the emitted dislocations remain pinned yet grow and accumulate underneath the indenter, where they interact and generate complex dislocation structures. Reactions among perfect dislocations under the indentation pit trigger nucleation of a few other partial dislocations with the Burgers vector of $\boldsymbol{b} = [0\bar{1}0]$, $\boldsymbol{b} = \frac{1}{3}[\bar{1}\bar{1}\bar{1}]$, and $\boldsymbol{b} = \frac{1}{6}[141]$. In general, perfect dislocations govern the plasticity of twin-free single crystal 3C-SiC.

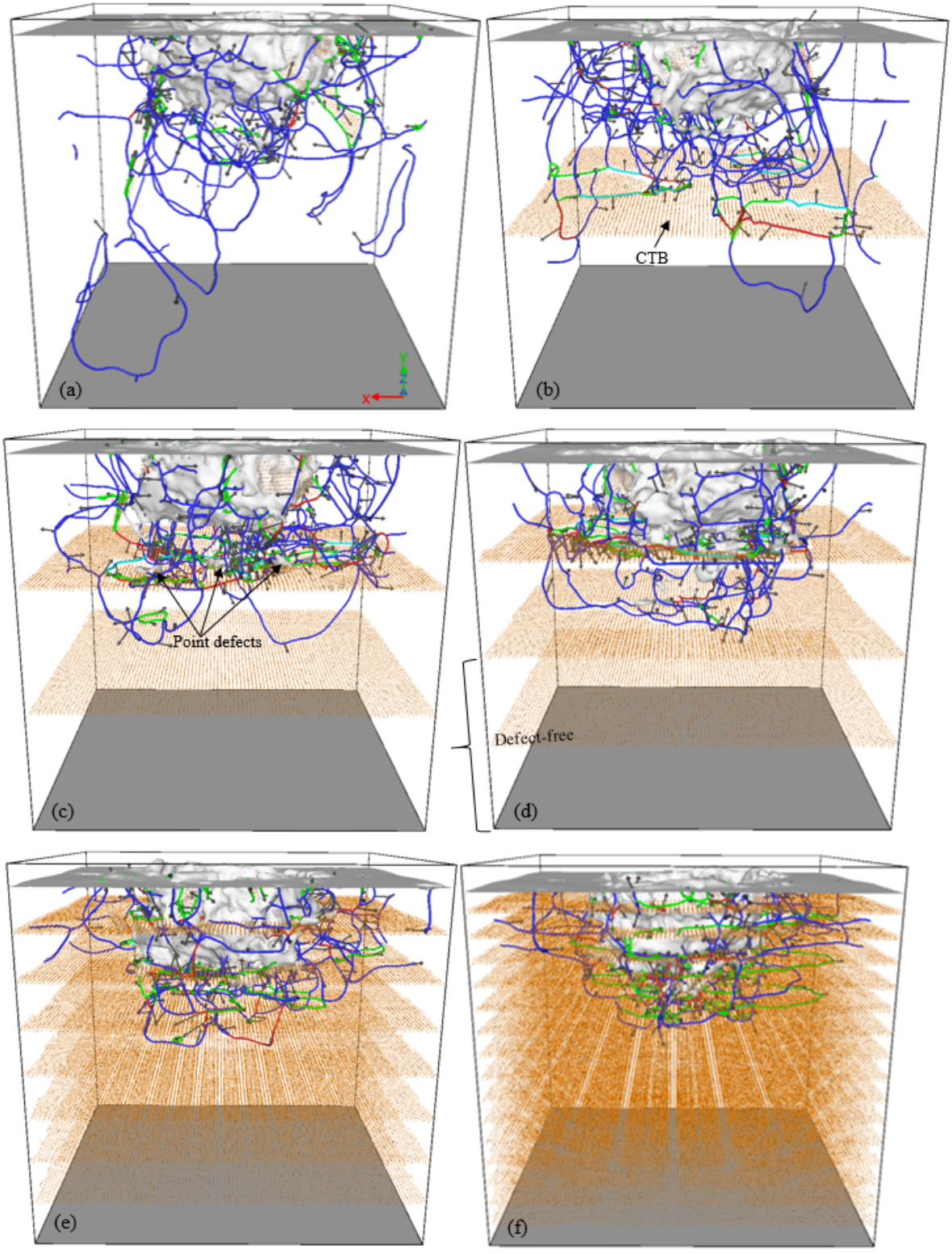

Figure 2 Overall defect network of indented single crystalline 3C-SiC substrate at h=6 nm. (a) Twin-free, (b) λ=12 nm, (c) λ=8 nm, (d) λ=6 nm, (e) λ=3 nm, (f) λ=1.5 nm. Dislocation lines are colored according to their Burgers vector i.e. blue, green, aqua, and red lines, respectively, represent the perfect, Shockley partial, Frank partial, and other partial dislocations. Black arrows designate directions of $\boldsymbol{b}$.

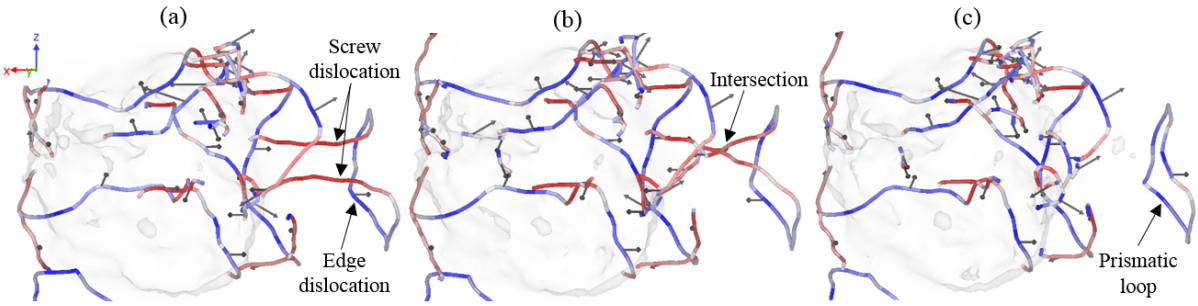

Figure 3 Formation of prismatic loop as a result of "Lasso"-like mechanism via intersection and annihilation of screw dislocations at h~1.8 nm. Dislocations are colored based on the dislocation character, with the screw components in red and edge components in blue.

Nanotwinned single crystal. As depicted in Figure 2, CTBs affect the defect network under the indentation pit, i.e. CTBs impede dislocation slip, mobility, and glide, due to the difference in the slip systems across a CTB, leading to the strong accumulations of dislocations between CTBs. Figure 4 shows that the dislocation density rises rather monotonically with indentation depth owing to the expansion of the plastic region as a result of evolving stress field beneath the indenter. However, the dislocation density does not reach a saturation state due to the imbalance of nucleation and annihilation rates. On the other hand, Figure 4a confirms that the nucleation rate of perfect dislocations in nanotwinned 3C-SiC is lower than that of the twin-free counterpart. Additionally, with the decrease of λ, the density of partial dislocations increases subject to further plastic strain imposed by the indenter, attributable to the dislocation interactions with the CTBs. Apparently, dissociation of perfect dislocations is more marked in the nanotwinned 3C-SiC with λ=1.5 nm, where the density of partial dislocations (3.2×10^{16} m^{-2}) exceeds that of the perfect dislocations (2.9×10^{16} m^{-2}).

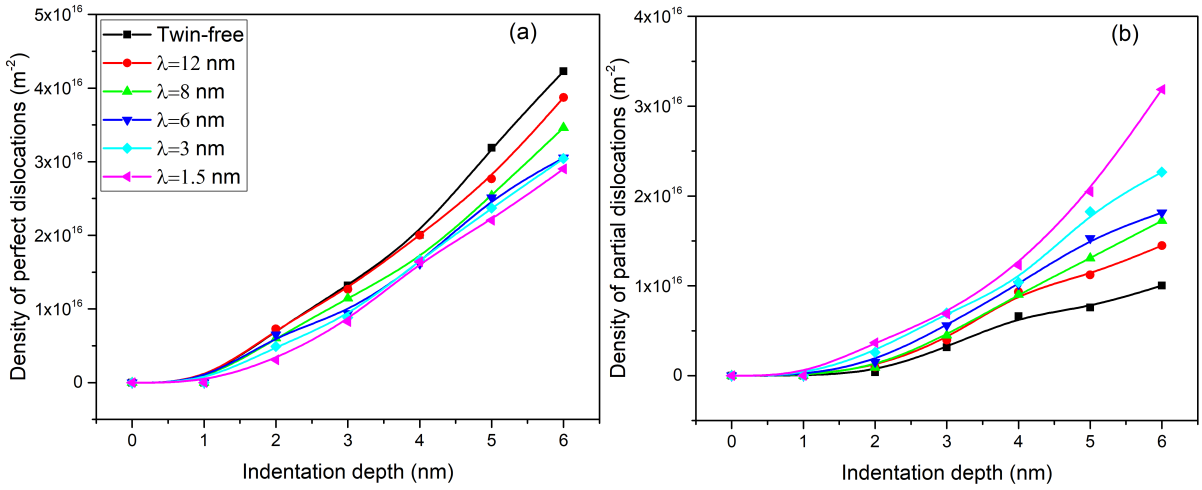

Figure 4 Evolution of density of (a) perfect and (b) partial dislocations with indentation depth in the single crystal substrates.

Dislocation-CTB interaction processes in the nanotwinned substrate with λ=12 nm are illustrated in Figure 5 and Figure 6. A prismatic loop with $\boldsymbol{b} = \frac{1}{2}[\bar{1}\bar{1}0]$ trapped in the CTB at *h*~3.8 nm is observed in Figure 5a. U-shaped half loops, comprising perfect dislocations gliding in the $\frac{1}{2}[011]$ and $\frac{1}{2}[\bar{1}0\bar{1}]$ directions, approach and then cross the {111} CTB. These incoming dislocations are initially repelled by the CTB due to the atomic structure of the boundary and the elastic anisotropy of the two crystals forming the CTB [63]. It is seen that when the dislocations reach the CTB, the dislocation lines become parallel to the intersection line of the slip plane and the CTB. The two U-shaped half loops gliding in the $\frac{1}{2}[011]$ first interact, generating a point defect and a dislocation junction with $\boldsymbol{b} = \frac{1}{2}[0\bar{1}\bar{1}]$ and $\boldsymbol{b} = \frac{1}{6}[\bar{4}1\bar{1}]$ at the CTB. As the indentation proceeds, the dislocation junction forms U-shaped half loops $\boldsymbol{b} = \frac{1}{2}[0\bar{1}\bar{1}]$ and $\boldsymbol{b} = \frac{1}{6}[4\bar{1}\bar{1}]$, as demonstrated in Figure 5b. These half loops dissociate within the CTB plane into Shockley partials $\boldsymbol{b} = \frac{1}{6}[\bar{2}1\bar{1}]$ and $\boldsymbol{b} = \frac{1}{6}[211]$, and Frank-type sessile partial $\boldsymbol{b} = \frac{1}{3}[\bar{1}11]$, propagating along the CTB. A partial dislocation segment $\boldsymbol{b} = [\bar{1}00]$ is transmitted across the CTB, as shown in Figure 5c. With the progress of indentation, more

Frank-type sessile partials $\boldsymbol{b} = \frac{1}{3}[\bar{1}11]$ nucleate and remain at the CTB. The transmitted partial dislocations across the CTB may recombine into a perfect dislocation $\boldsymbol{b} = \frac{1}{2}[101]$, indicated in Figure 5d. Figure 6 provides a zoomed view on the CTB to present the detailed atomic structure of the CTB at the moment of dislocation interaction and transmission. Upon approaching the perfect dislocation to the CTB, the CTB structure is slightly distorted. With increasing indentation depth, and in turn higher resolved shear stress (RSS) on the CTB plane, the CTB is moved towards the negative *Y* direction by two atomic planes, with twinning partial dislocations, comprising Frank dislocations and Shockley partials, at the CTB accompanied by a step, as displayed in Figure 6c and 6d. The propagation and glide of twinning dislocations along the CTB plane trigger formation of steps which may eventually initiate CTB migration (in the direction perpendicular to the CTB) downward by two atomic layers. A similar mechanism of twinning dislocation has been reported in fcc metals, which is indeed driven by shear stress parallel to the CTB plane, rendering a favourable Peach-Koehler force on the twinning dislocations [64, 65].

It is of note that the U-shaped half loop with $\boldsymbol{b} = \frac{1}{2}[\bar{1}0\bar{1}]$ shown on the right hand side of Figure 5a is reflected back and does not dissociate at the CTB up to maximum indentation depth in our work. However, this U-shaped half loop is eventually transmitted across the CTB through the dislocation reactions at the CTB including nucleation of twinning partial dislocations (Shockley partials, Frank-type sessile partials, and other unknown partials, along with associated steps) confined inside the CTB and propagating within the CTB. Formation and annihilation of point defects adjacent to the CTB are also observed before the transmission. As demonstrated in Figure 6d and Figure 6e, lattice dislocations emitted from the defective CTB at the sites of the steps grow by nucleating an ISF which is dragged behind. In view of these results, we conclude that the formation of point defects and twinning partial dislocations

dominate the transmission mechanisms in the nanotwinned 3C-SiC. Such an interaction process might be assumed as a stress-driven transmission process in a perfect diamond lattice.

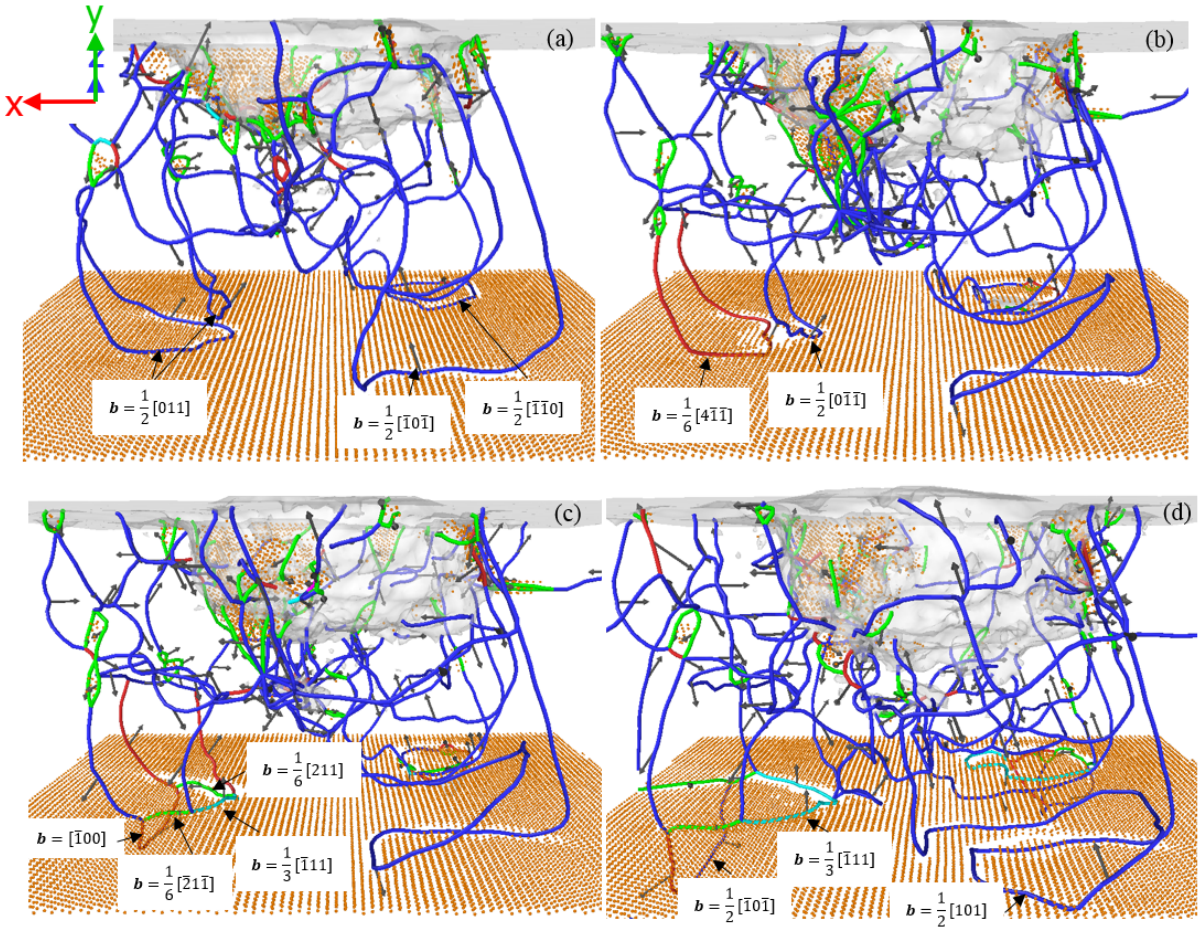

Figure 5 Dislocation-CTB interaction in the nanotwinned 3C-SiC substrate with λ=12 nm.

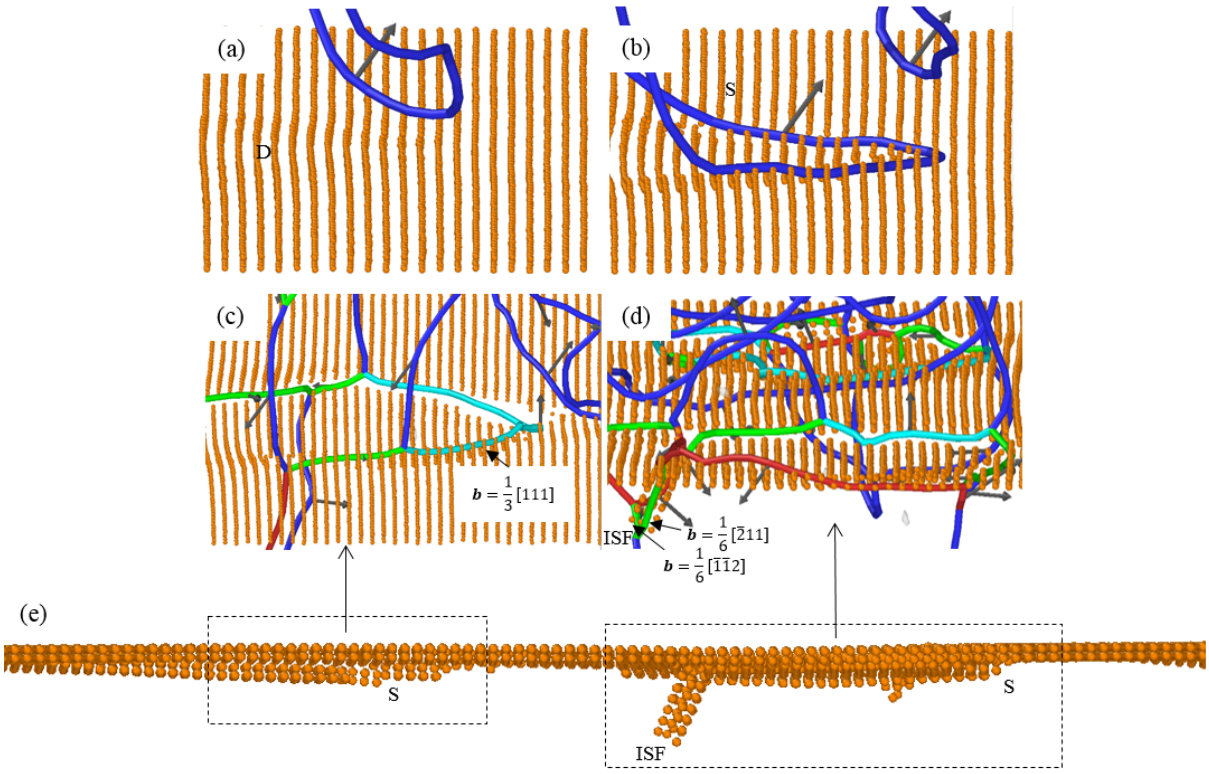

Figure 6 (a-d) Detailed atomic structures of CTB in the nanotwinned 3C-SiC substrate with λ=12 nm, (e) Side view of the CTB showing the formation of steps and nucleation of a Shockley partials accompanied by a stacking fault from the defective CTB. D, distortion of the CTB due to the incoming dislocations; S, slip; ISF, intrinsic stacking fault.

As illustrated in Figure 2c, in the nanotwinned substrate with λ=8 nm, the first CTB severely blocks dislocation migration, leading to the accumulation of dislocations at the first CTB. Among all dislocations transmitted across the first CTB, only a few marginally interact with the second CTB yet without any transmission process, suggestive of the insufficient RSS on the CTB plane to activate twinning partial dislocations. Several point defects, twinning dislocations including Frank-type sessile partials with $\boldsymbol{b} = \frac{1}{3} < 111 >$, Shockley partials $\boldsymbol{b} = \frac{1}{6} < 211 >$, and other partials, e.g., $\boldsymbol{b} = \frac{1}{6}[215]$ and $\boldsymbol{b} = \frac{1}{6}[\bar{1}\bar{1}\bar{4}]$, together with steps are formed within the first CTB, which make it utterly defective. The dislocation-CTB interaction and transmission mechanisms for the other nanotwinned 3C-SiC substrates with smaller λ are found to be identical to the former cases (see Supplementary Movie 2), attributable to the presence of the same Σ3 CTB as well as the nature of the incoming perfect dislocations.

However, with decreasing λ, twinning dislocation occurs via dissociation and propagation of mostly Shockley partials rather than Frank partials trapped at the CTB. The Shockley partials can expand along the CTB plane to form half-loops, as seen in Figure 2e and Figure 2f. In other words, if λ is reduced, the Frank-type sessile partials could become less prone to nucleation within the CTB plausibly due to high levels of RSS on the CTB. Note that direct slip transmission of dislocations across the CTB is not observed in our simulations. In fact, direct slip transmission in any crystalline materials is rarely observed in atomistic simulations [66]. Besides, since the indentation direction is perpendicular to the CTBs, CTB migration does not occur primarily due to the lack of large enough RSS, although some steps are formed at the CTBs.

3.2. Deformation characteristics of nanocrystalline 3C-SiC

Figure 7 provides an overview of the dislocation network for some representative cases of the twin-free and nanotwinned nanocrystalline 3C-SiC at h=6 nm, where complex dislocation networks at the GBs and dislocation segments inside individual grains are observed. In this section, we first describe how plastic deformation transpires in twin-free nanocrystalline 3C-SiC, covering the effect of pre-existing dislocations at the GBs, incipient dislocation activity, intergranular and intragranular deformation mechanisms. We then provide relevant discussion for the twinned nanocrystalline samples.

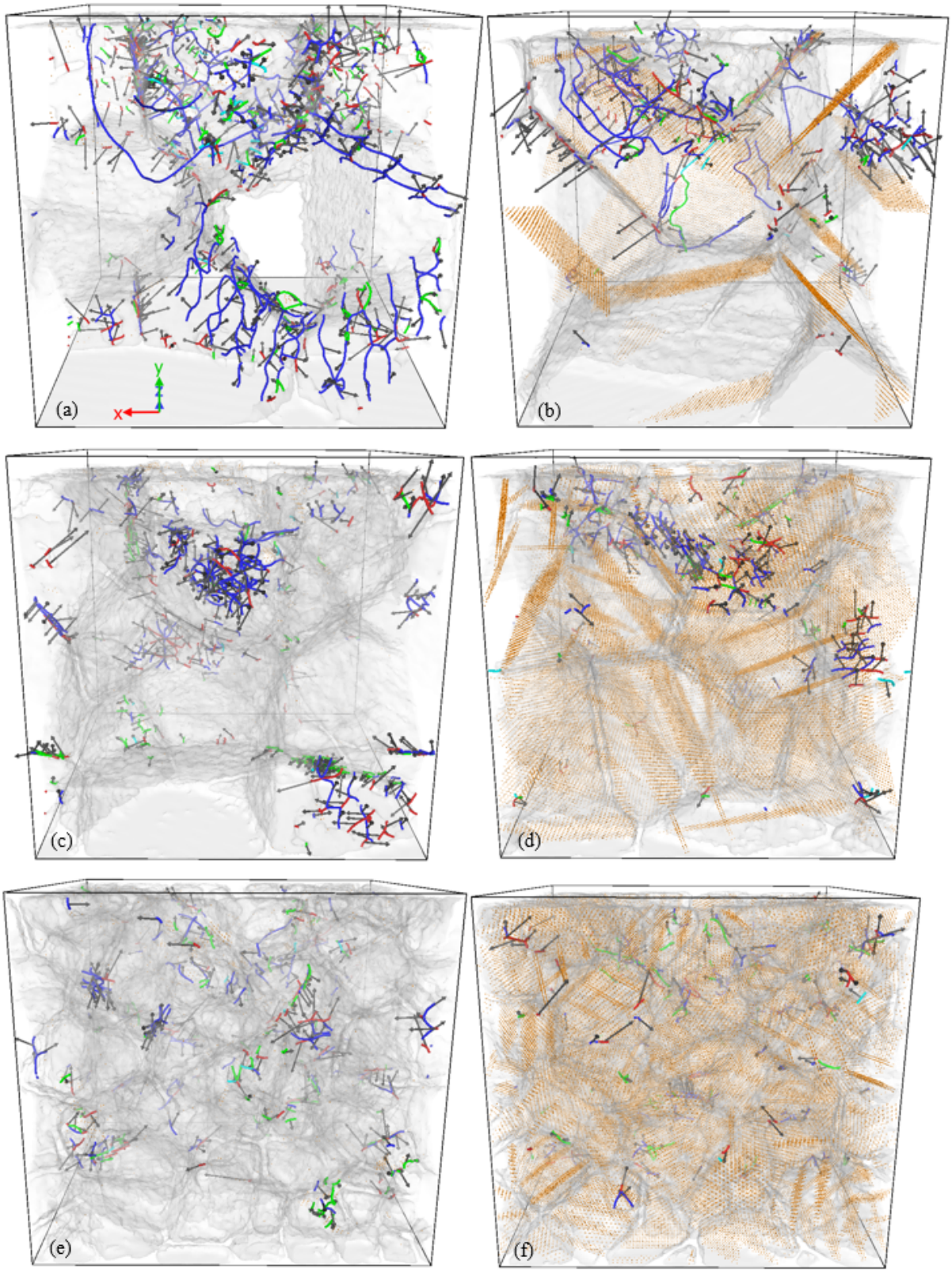

Figure 7 Snapshots showing the dislocation network inside the nanocrystalline 3C-SiC at h=6 nm, for some representative cases (a-b) Twin-free and nanotwinned (λ=8 nm) samples with d=15 nm, (c-d) Twin-free and nanotwinned (λ=3 nm) samples with d=8 nm, (e-f) Twin-free and nanotwinned (λ=1.5 nm) samples with d=4 nm.

Twin-free nanocrystalline 3C-SiC. Figure 8 shows side views of the twin-free nanocrystalline 3C-SiC substrates before indentation. There exist pre-existing partial and perfect dislocations at the GBs which are inherently formed during building nanocrystals. We emphasize that the pre-existing dislocations are intrinsic which cannot be removed by dynamic relaxation, energy minimization, and high-temperature annealing. The pre-existing dislocations include distinct types of single segments and multiple junctions. Intriguingly, some of these pre-existing dislocations exhibit starfish-like, spider-web-like, and ladder-like shapes, featuring a low angle GB. Pre-existing spider-web-like dislocation network was also observed in polycrystalline bcc iron [67]. Note that low angle GBs are exhibited by dislocation network while high angle GBs are not. However, pre-existing dislocations may exist in both low angle and high angle GBs. The pre-existing dislocations could act as dislocation sources, and they could be activated and migrate by overcoming the Peierls stress during the deformation process. It is realized from Figure 8 that the density of pre-existing dislocations is dependent on the grain size, i.e. decrease of density of pre-existing dislocations with grain size. To quantify the density of pre-existing dislocations, we define the density of "full" dislocations as: Full dislocation density = (perfect dislocation line length + (partial dislocation line length / 2)) / system volume. Figure 8d proves that the density of full pre-existing dislocations decreases from 4.3×10^{16} m^{-2} to 1.3×10^{16} m^{-2} in the twin-free nanocrystal when d reduces from 15 nm to 4 nm. To realize the probable interaction of stress between the pre-existing dislocations and those dislocations nucleating from the GBs, the net stress field of pre-existing dislocations in the twin-free samples is calculated as $Gb/2\pi r$, where G is the shear modulus (G=123.7 GPa for 3C-SiC [46]), b is the net magnitude of spatial Burgers vectors, and r is approximately the distance between the GB dislocation and the lattice dislocation. It should be mentioned that the real net Burgers vector requires information of the line sense of all dislocations as well as the crystal orientations of all grains in which each dislocation sits in. However, it is difficult to have this

information because most GB dislocations sit right between two grains. However, the net spatial Burgers vector can be a crude first-order estimation for calculating the net stress field of pre-existing dislocations. Also, the accurate interaction stress depends on the interaction distance, yet it would be difficult to have this information for each and every pre-existing GB dislocation. Thus, we let *r* be the average grain size *d* in this study. The net stress filed per grain is estimated to be around 0.14 GPa, 1.48 GPa, and 4.6 GPa, respectively, for the samples with *d*=4 nm, *d*=8 nm, and *d*=15 nm.

It is worth nothing that the relaxation methodology of the GBs before performing nanoindentation could influence the density of pre-existing GB dislocations and mechanical response of material. A dummy nanoindentation simulation on high-temperature annealed twin-free sample with *d*=8 nm, which essentially has a different density of the pre-existing GB dislocations, $4.1 \times 10^{16}\ \mathrm{m}^{-2}$, demonstrated that the average nanoindentation hardness (See section 3.4) is ~7% higher than that of shown in Figure 8. This observation indicates that the pre-existing GB dislocations does not affect the average nanoindentation hardness, otherwise the sample with higher pre-existing GB dislocations might have had lower indentation hardness. The higher hardness arises from high-temperature annealing which dissipates energy and reduces the average atomic energy of the system [56, 68]. Nevertheless, exploring the effects of initial GB structure is out of the scope of the current contribution.

Further analysis of dislocation density graph in Figure 8 unveils a low level of dislocation activity in the twin-free nanocrystal with small grain sizes, implying that the plastic strain energy is primarily released by the GB-associated processes during the indentation. GB-based plasticity mechanisms, mainly GB sliding, are driven by rotational or translational strain jumps [69]. GB sliding can affect the total shear stress applied to the substrate, i.e. it decreases the total shear strain by accommodating most of the shear strain imposed by the indenter, thus reducing the transferable amount of strain into the grain interior, leading to low dislocation

activity and mobility inside the grains. However, the GB sliding effects lessen with increasing grain size.

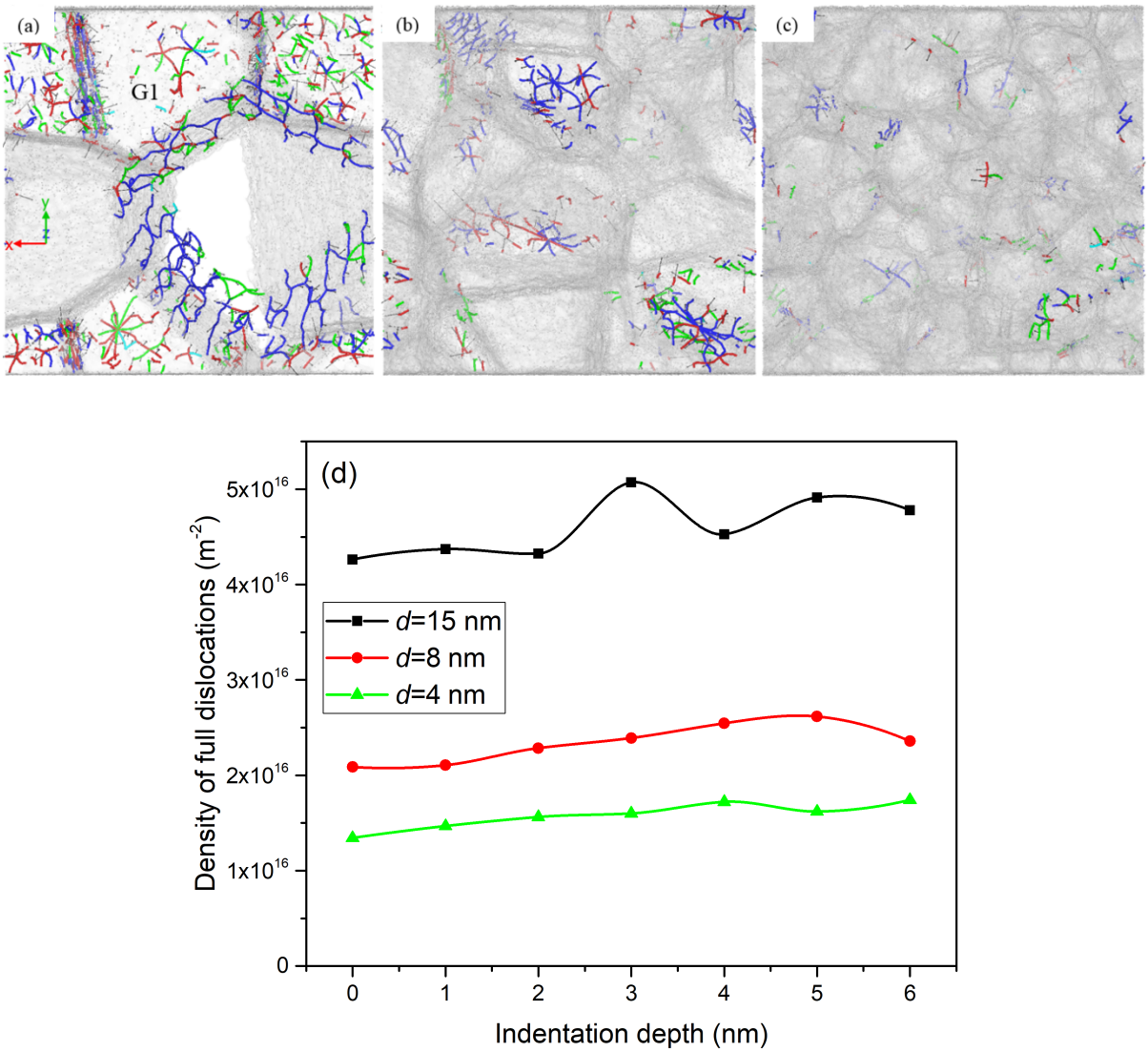

Figure 8 Pre-existing dislocations at the GBs of the twin-free nanocrystalline substrates with (a) d=15 nm, (b) d=8 nm, (c) d=4 nm; (d) Density of full dislocations as a function of the indentation depth.

To gain further insight into the dislocation activity in the grain lying directly under the indenter, the grain labeled G1 in Figure 8a is selected for the analysis. As shown in Figure 9, some dislocation activities can be seen at GBs of G1, i.e. repetitive nucleation and annihilation of partial and perfect dislocations forming triple and multiple junctions at h=0.1 nm. It is observed in Figure 9c that a starfish-like dislocation structure is generated at the GB 1-2 at h=0.7 nm,

which is dissociated with further progress of indentation. At h~1.3 nm, first lattice dislocation, as a perfect dislocation, is successfully emitted from the indentation pit, gliding in the $\frac{1}{2}[1\bar{1}0]$ direction. The dislocation nucleation within the G1 grain initiates at similar h to that in the twin-free single crystal. The nucleated perfect dislocation forms a half-loop and starts to propagate until it reaches the GB, which serves as a dislocation sink by absorbing the dislocation. A perfect dislocation $\boldsymbol{b} = \frac{1}{2}[\bar{1}10]$ is also nucleated from the indentation surface, before moving toward and being absorbed by the GB. Further dislocation emission and propagation occurs in G1 at deeper indentation depths, which is accompanied by the activation of some pre-existing dislocation embryos at the GBs. Note that as the indentation proceeds, some of the pre-existing dislocations in the adjacent grains are activated and slowly grow into the interior of the grains to reach the opposite GB unobstructedly. In the meantime, some lattice dislocations are heterogeneously emitted from the GBs in the vicinity of the indentation region. However, no lattice dislocation nucleation happens in grains that are far from the indentation pit, where the RSS is too low to trigger nucleation of dislocations from the GBs. It should be noted that, similar to the single crystal cases, only perfect dislocations nucleate in G1. Besides, stacking faults are not found in the grains for the studied cases, attributable to the limited emission and growth of partial dislocation slip inside the GBs. Simulations also show that the process of dislocation nucleation in the twin-free nanocrystals is not considerably affected by the pre-existing GB dislocations.

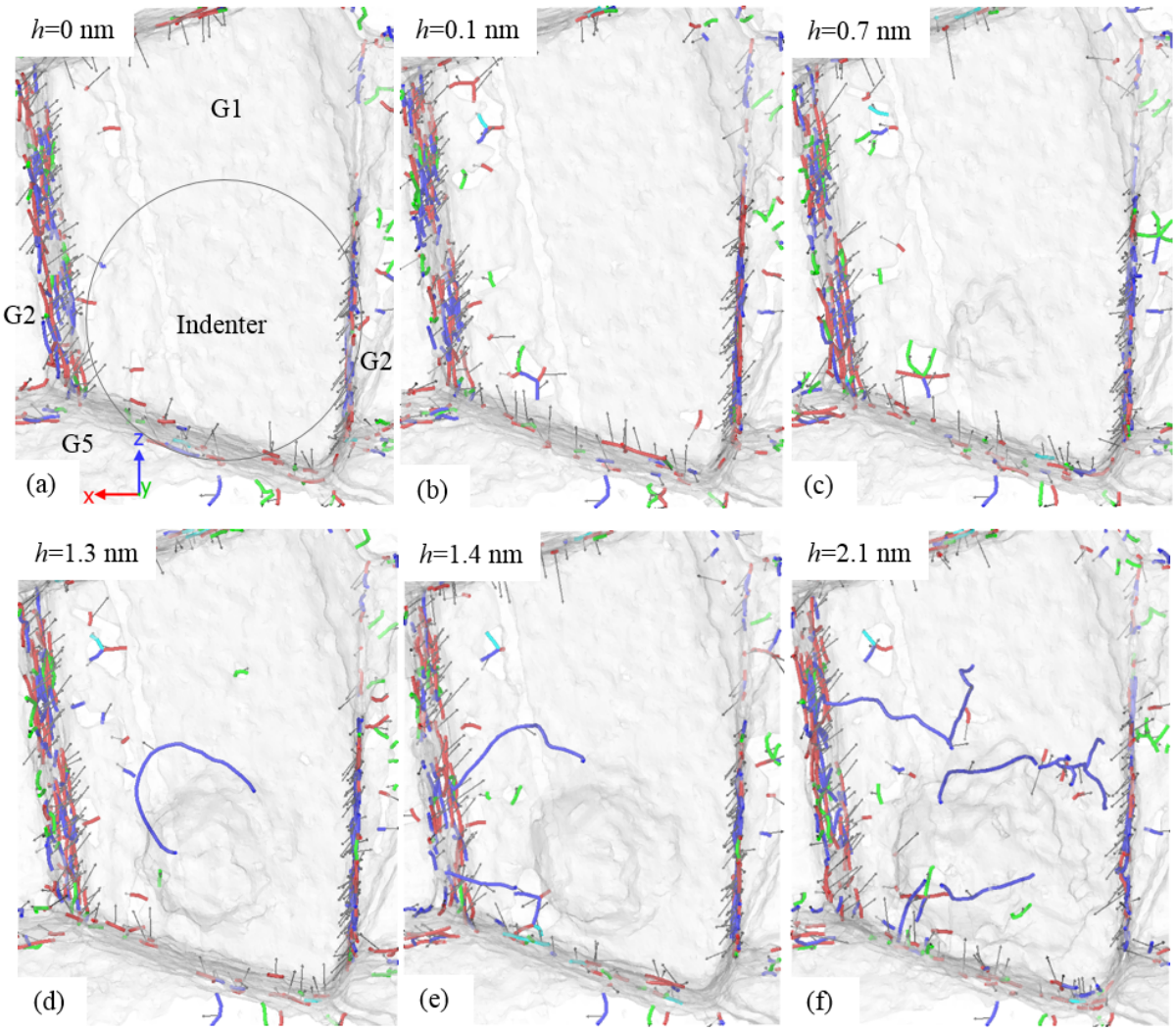

Figure 9 Incipient of dislocation activity in the grain lying directly under the indenter (G1) for the nanocrystalline substrate with d=15 nm.

Figure 10a-c shows that there are two coexisting phases in the nanocrystalline 3C-SiC, i.e. crystalline intragranular (in blue) and disordered intergranular (in white) phases. The soft disordered phase in GBs could essentially control the material's mechanical response [33]. To investigate the relation between the grain size and crystallinity of the nanocrystalline substrates, the fraction of disordered intergranular phase is measured and compared with that of the single crystal. It is observed from Figure 10d that the fraction of disordered intergranular phase increases with the decrease of grain size, leading to the enhancement of the plasticity (see Section 3.4). On the other hand, increasing the volume fraction of GBs triggers the deformation

physics to shift to interface-mediated mechanisms involving interactions among GB sliding and dislocation plasticity. It can be realized that ~1% of atoms undergo the transition from crystalline to disordered phase in the substrates with different grain sizes examined in this study. Notably, in the twin-free single crystal substrate, ~3.5% of atoms experience the transition to the disordered state, giving rise to the dominance of disordering and dislocation plasticity mechanisms. Another observation is the GB and triple junction migration between G1 and G2 in the region of highly localized strain under the indenter in the 15 nm grain size sample, as shown in Figure 10b-c. This process can facilitate local reorientation of the lattice in the grains. With the increase of h up to 6 nm, grain coalescence does not occur completely as G1 and G2 do not undergo a cooperative rotation to generate a single large grain. Away from the indentation pit, grains preserve their size and shape as the unindented structure, confirming that intragranular and intergranular mechanisms are confined to the region directly underneath the indenter, where high compressive and shear stresses are imposed. GB thickening transpires for the GB 1-4 and GB 3-4, which is explained by the motion of intragranular atoms nearby the GBs and transformation to the disordered phase. On the other hand, GB 1-2 and GB 1-3 become thinner. GB thickening/thinning in the grains adjacent to the region of highly localized strain can be considered as a ubiquitous deformation mode in nanocrystalline materials [68], suggestive of accumulation of some plastic strains in the GBs and local disordered atoms around the GBs. It should be noted that GB thickening/thinning is also observed for the 8 nm and 4 nm grain size samples, yet grain coarsening is not found in these cases either. In particular, the GB thickening increases with decreasing grain size.

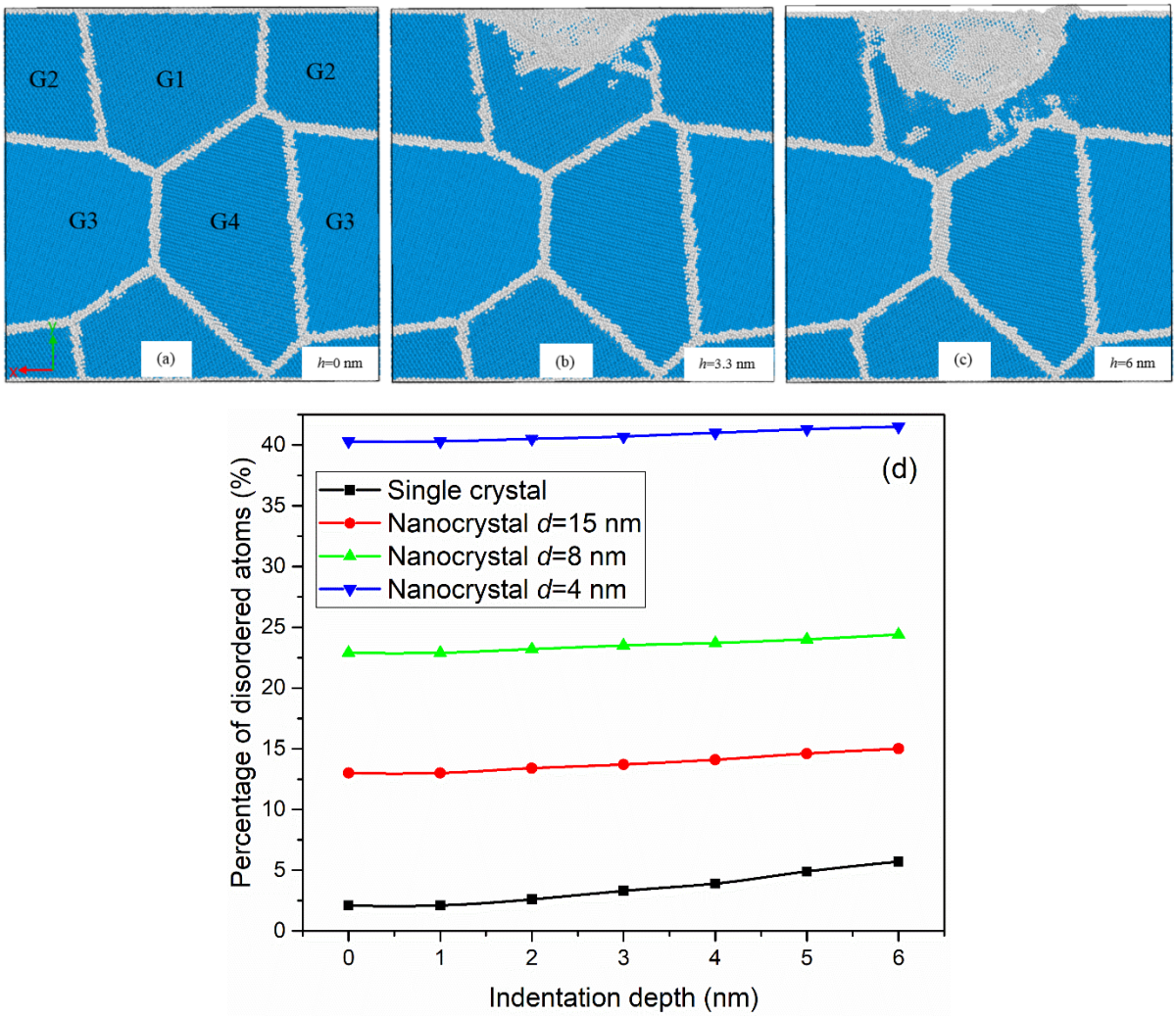

Figure 10 (a-c) Crystalline intragranular (in blue color) and disordered intergranular (in white color) phases in the nanocrystalline 3C-SiC with d=15 nm, (b-c) GB and triple junction migration between G1 and G2, (d) Percentage of disordered atoms as a function of indentation depth.

Local von Mises shear strain [70] can reflect the relative displacement of atoms, thus, this invariant is adopted to further analyze the local deformation history and track the trajectory of atomic deformation mechanisms. In Figure 11, the GBs and traces of dislocation slipping possess relatively high magnitudes of shear strain (in ivory color) as compared to the surroundings. As Figure 11 illustrates, for larger grains, e.g., d=15 nm and d=8 nm, the deformation and slip systems are localized in one or two grains and GBs, which compensate the strain applied by the indenter. However, in the case of small grain with d=4 nm, more GBs

cooperate in absorbing the indentation deformation which results in a wider distribution of shear strain. Figure 11 suggests that as the mean grain size decreases, a transition from the dislocation-based to GB-mediated plasticity occurs. This observation can be considered as an inverse Hall-Petch effect [71], where intergranular mechanisms dominate the plasticity of the nanocrystalline material. In fact, in a substrate with large grains (of the order of 8 nm), the intergranular mechanisms, e.g., GB sliding, GB migration, and GB rotation accompanied by intragranular deformation mechanisms, e.g., dislocation slipping activities in multiple grains control the plastic deformation of the nanocrystalline material under the nanoindentation loading. However, in a substrate with small grains, e.g., 4 nm, the trace of dislocations is absent, as demonstrated in Figure 11c. Thus, it can be deduced that the dislocation activity within nanoscale grains under the indenter decreases with the grain size.

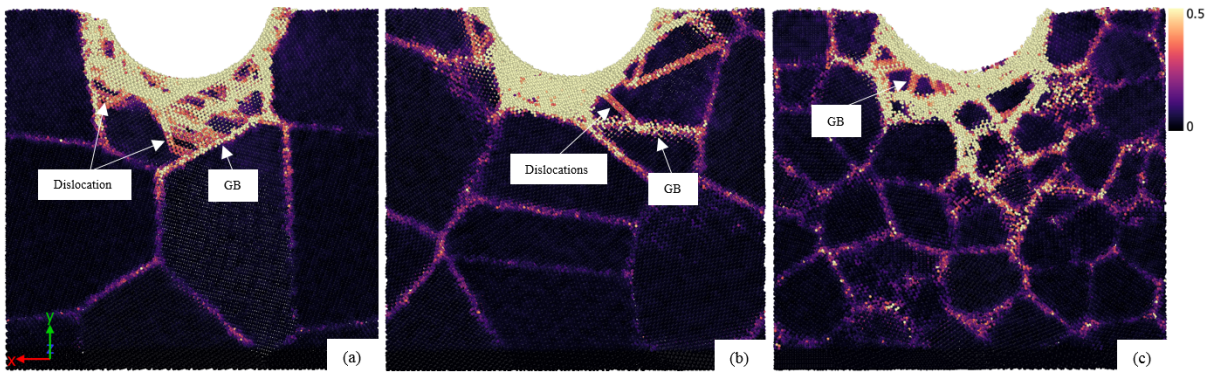

Figure 11 Local shear strain distribution in the XY plane in the twin-free nanocrystalline substrates with (a) d=15 nm, (b) d=8 nm, and (c) d=4 nm, respectively, at h=5 nm.

Nanotwinned nanocrystalline 3C-SiC. Inspection of the MD snapshots of the nanotwinned nanocrystalline 3C-SiC with λ=1.5-12 nm unveils a stochastic formation and distribution of pre-existing partial and perfect dislocations at the GBs. As Figure 12 shows, nanotwinned nanocrystalline with d=15 nm and varying λ comprises of the lowest pre-existing full

dislocation density, i.e. $2 \times 10^{15} - 5 \times 10^{15}$ m^{-2}, among the studied cases, which is in contrast to that of the twin-free nanocrystal with the same grain size, where the twin-free nanocrystal with *d*=15 nm shows the highest level of pre-existing full dislocation density. Irrespective of the λ, the density of pre-existing full dislocations in the twin-free nanocrystal with *d*=8 nm and *d*=4 nm is also found to be higher than their nanotwinned counterparts. Figure 12 also evidences that limited lattice dislocation slip transpires in the grains of the nanotwinned nanocrystal with *d*=4 nm during the indentation process, pointing out to the high activity of intergranular deformation processes. In fact, similar to the twin-free nanocrystals with small grain sizes (of the order of 4 nm), dislocation activity in nanotwinned small grain nanocrystals is mainly restricted to the dissociation, nucleation, and annihilation of pre-existing dislocations, which are far from the high stress zone under the indenter, thus, they hardly contribute to the plasticity of the substrate. Notice that no specific trend is found for the density of pre-existing full dislocations as well as their evolution during the indentation as a function of λ. The simulation data also demonstrate that the CTB density could affect the resulting dislocation activity, i.e. the partial dislocation density in the grains would be higher than that in the twin-free nanocrystals, in consistent with the observations of the single crystals discussed in Section 3.1 as well as findings on the nanotwinned nanocrystalline Cu under uniaxial strain [72].

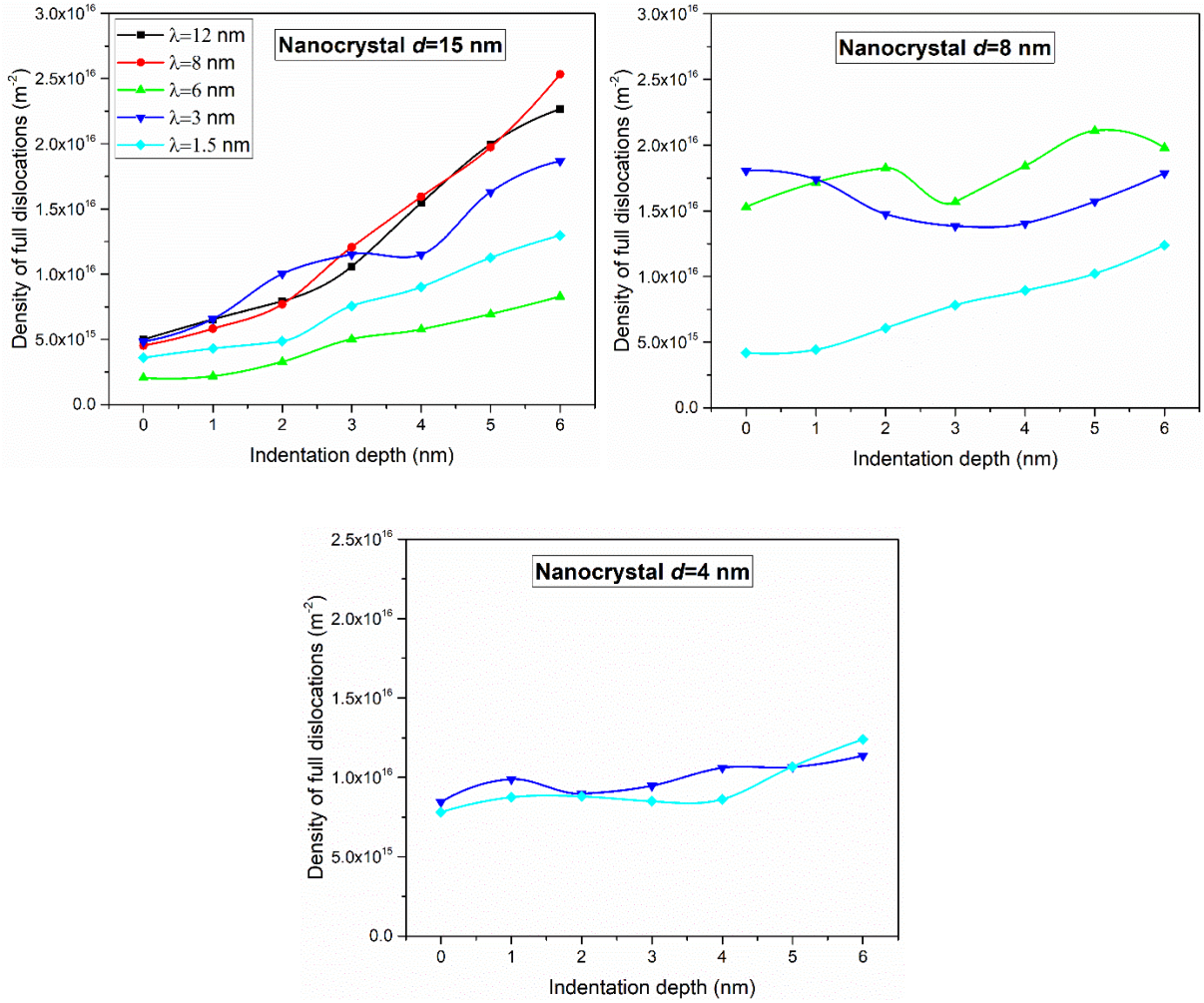

Figure 12 Density evolution of full dislocations with indentation depth for the nanotwinned nanocrystalline 3C-SiC.

Figure 13 provides the microstructure at h=5 nm where atoms are colored according to their local von Mises invariant shear strain. It is found that, regardless of λ, GBs, lattice dislocation glide, and CTBs collectively accommodate the imposed plastic strain by the indenter in the nanocrystalline substrates with d=15 nm, however, with the decrease of d, the contributions of lattice dislocations and CTBs become limited. Particularly, in the substrates containing large grains, i.e. $d \geq 8$ nm, the contribution of CTBs to plastic deformation is more pronounced than that of the smaller grains, signifying that in highly twinned nanocrystalline microstructures with a large enough grain (of the order of 8 nm), CTBs can accommodate a fraction of imposed

shear strain thus contributing to the plasticity. However, in substrates with small grains, e.g., d=4 nm, CTBs and lattice dislocations have trivial influence on the deformation plasticity. Simulations suggest that when the grain size is small enough (of the order of 4 nm), GBs accommodate the majority of strain, meaning that the GB processes, e.g., GB shear, are the primary plasticity mechanism in this case, which can result in the inverse Hall-Petch effect. This finding is consistent with the former results of nanocrystalline Cu and Ni with d=5 nm, where the plastic deformation were governed by GB accommodation mechanisms [73, 74].

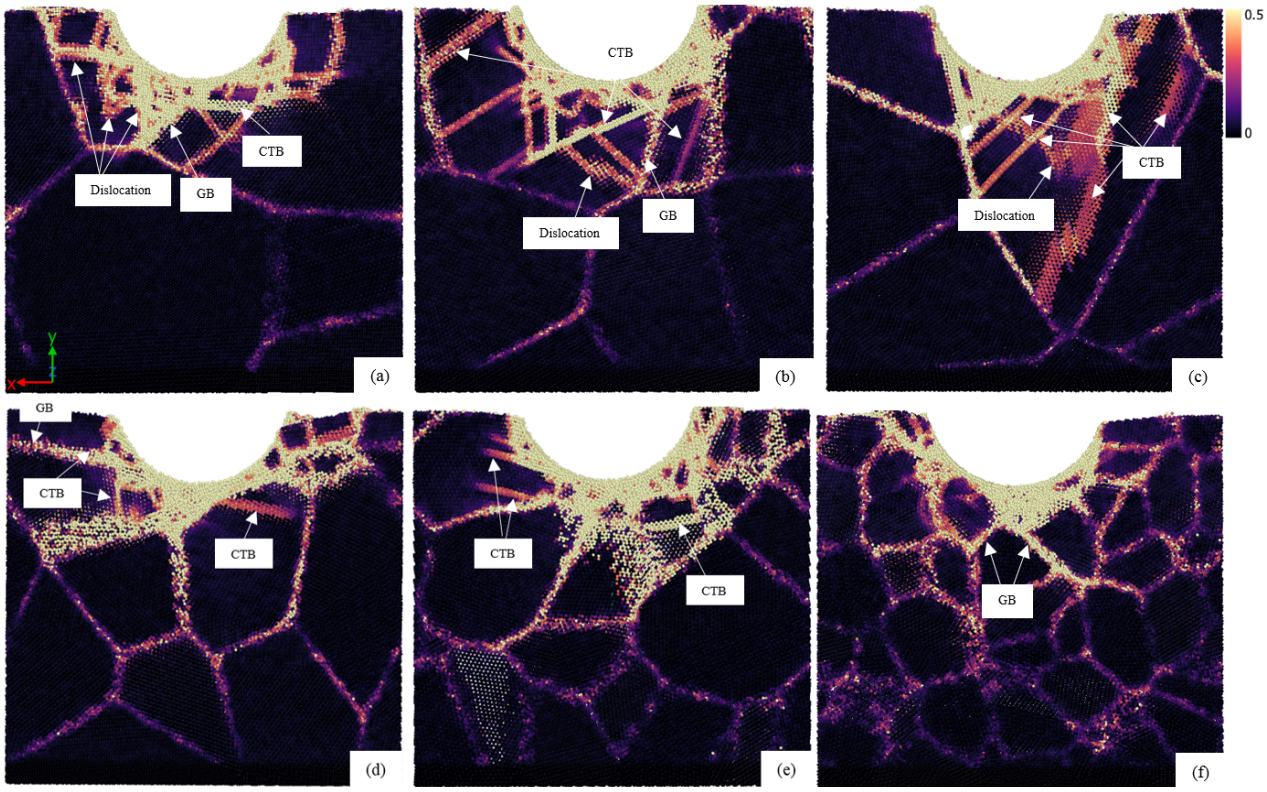

Figure 13 The microstructures of the nanotwinned nanocrystalline substrates in the *XY* plane under indentation at h= 5nm. Atoms are colored according to their local shear strain, (a) d=15 nm, λ=12 nm, (b) d=15 nm, λ=6 nm, (c) d=15 nm, λ=1.5 nm, (d) d=8 nm, λ=6 nm, (e) d=8 nm, λ=1.5 nm, (f) d=4 nm, λ=1.5 nm. A one-to-one comparison with the DXA snapshots is carried out to distinguish lattice dislocations from CTBs, which are both appeared in ivory color.

In the nanotwinned nanocrystalline substrate with d=15 nm and λ=12 nm, plastic deformation initiates with the emission of perfect dislocations in the high stress region underneath the indenter, which is similar to the twin-free single crystalline and nanocrystalline cases. In

particular, grains located directly beneath the indenter encompass higher dislocation concentration than the others, simply because of the higher levels of imposed stress experienced by the individual grains. Nevertheless, crystallographic orientation of the grain can also affect the dislocation activity within it. As seen in Supplementary Movie 3, the motion of a nucleated perfect dislocation from the indentation pit surface within the grain is blocked by the CTB. In fact, the grain interior is transected by the CTB, giving rise to inhibiting further dislocation propagation. The perfect dislocation is seen to glide within the CTB in the grain and it is dissociated and recombined at the CTB. The perfect dislocation continues to glide at the CTB, then instead of being transmitted across the CTB, it is reflected back to the grain, before eventually being absorbed by the opposite GB. However, there exist other perfect dislocations that are transmitted across the CTB following nucleation and gliding of twinning partial dislocations confined inside the CTB. The CTBs are also observed to act as preferred emission pathways for dislocations nucleated from the intersection of the CTB and indentation pit, primarily owing to the local high stress concentration, similar to the sites of the CTB-GB intersections [6]. Further investigations suggest that such dislocation activities also occur in other nanotwinned nanocrystalline substrates with d=15 nm yet with smaller λ.

Supplementary Movie 4 shows the dislocation activity in the nanotwinned nanocrystalline substrate with d=8 nm and λ=6 nm. As mentioned previously, dislocation activity is suppressed in the substrates with a high density of CTBs, as compared to the twin-free case and the substrates with a low density of CTBs, indicating that CTBs could act as obstacles to dislocation nucleation and motion. Moreover, irrespective of λ, very limited dislocation slip around the indentation pit is observed in the grains of the substrate with d=4 nm. A closer look at the simulation results reveals the lack of stacking faults in the nanotwinned nanocrystalline substrates, similar to the twin-free nanocrystal. According to the shear strain and lattice dislocation slip analysis, it can be concluded that during the incipient plasticity in the

nanocrystalline substrates with $d \geq 8$ nm, emission/multiplication of perfect dislocations from the penetrated surface within individual grains occurs, followed by the contribution of GBs and CTBs to the plasticity, yet, in substrates with smaller grains, incipient plastic deformation is carried by the GBs sliding adjacent to the indentation pit.

3.3. Influence of indenter size, temperature, and indentation speed on the plasticity mechanisms

The nanoindentation responses of materials may be dependent on the test conditions, e.g., temperature and indentation speed [42, 47]. Having examined the deformation mechanisms of twin-free and nanotwinned single/nanocrystalline 3C-SiC under nanoindentation loading, we now turn our attention to unraveling the effect of indenter size, temperature, and indentation speed on the above-reported plasticity mechanisms.

Indenter size. To study the effects of indenter size, we select the nanotwinned single crystal sample with λ=3 nm and the nanotwinned nanocrystalline substrate with d=8 nm and λ=3 nm as the representative cases at T=300 K and indentation speed of 50 m/s. The indenter radius varies from 4 to 8 nm. It is sensible to assume that a large indenter can generate a large volume stress field, relative to a small indenter, which could lead to formation of a large defect structure. Figure 14a-c compares the defect structure under the indenter at the initial stage of plasticity for three different indenter sizes. Formation and annihilation of point defects underneath the indenter occur for all indenter sizes. However, more point defects are emitted while applying larger indenters. Also, the defect structure is found to extend over a larger region than for the small indenter, consistent with the observations of Knap and Ortiz [75]. Also, the onset of plasticity takes place at lower indentation depth for the smaller indenter. Further analysis shows that the indenter size does not affect the dislocation-CTB interaction mechanisms.

Figure 14d-g depicts the indentation results of the nanotwinned nanocrystalline using small indenter R=4 nm, where very few heterogeneous dislocation activities in the adjacent grain interior are observed. A close look at the von Mises shear strain distribution, shown in Figure 14f, reveals that the indenter first indents the GB, and the two grains are subsequently crushed apart. Thus, higher shear strains are observed in the GBs directly beneath the indenter, suggesting that the onset of plasticity is dominated by the GB-mediated mechanisms. Figure 14g demonstrates the indented nanocrystalline sample at h=4 nm, where traces of a dislocation slip and CTBs are seen. In the case of a larger indenter R=8 nm, shown in Figure 14h-k, more lattice dislocation segments are nucleated under the indentation pit, however, the von Mises shear strain analysis confirms that GBs and CTBs mostly accommodate the plastic strain; thus in our simulations, nanoindentation plastic deformation of the nanotwinned nanocrystals with d=8 nm using small and large indenters is identically dominated by GBs and CTBs, with some contributions from lattice dislocations.

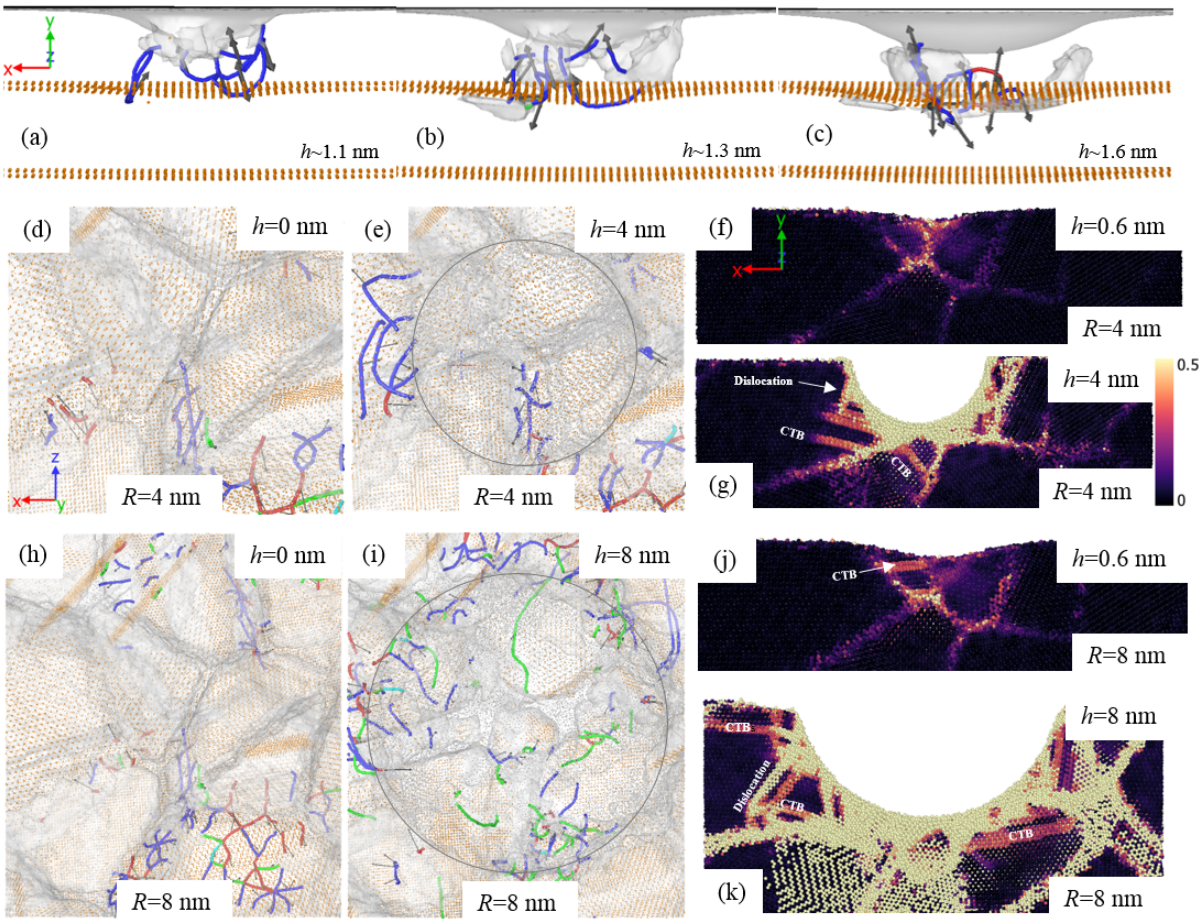

Figure 14 Defect structure of nanotwinned single crystal with λ=3 nm under the indenter at the initial stage of plasticity for the indenter sizes of (a) *R*=4 nm, (b) *R*=6 nm, (c) *R*=8 nm; (d-i) and (f-k) Defect structure and von Mises shear strain distribution of the nanotwinned nanocrystal with *d*=8 nm and λ=3 nm in the *XY* plane, respectively, with different *R*.

Temperature. To explore the influence of temperature, twin-free and nanotwinned single crystals and nanocrystalline samples with *d*=8 nm, and λ=12 and λ=3 nm, indentation speed of 50 m/s and *R*=6 nm are selected. The temperature varies from 10 to 2000 K. With the increase of temperature, the onset of plasticity, i.e. nucleation of the first dislocation, is seen to shift to the lower indentation depths regime, confirming the thermally-activated nature of defect formation. Simulation results of the twin-free single crystal at 10 K indicates that same "Lasso"-like mechanism of prismatic loop formation via intersection and annihilation of screw dislocations occurs at low temperatures. However, formation of first prismatic loops takes

place at deeper indentation depths at low temperatures, e.g., at h~2.3, 1.8, 1.7, and 1.3 nm for the temperatures of 10, 300, 600, 1000, and 2000 K, respectively. In general, the emitted prismatic loops are ~16-25 nm long at the stage of pinching off. It can be assumed that the "Lasso"-like mechanism of prismatic loop formation via intersection and annihilation of screw dislocations is associated with the augmented dislocation nucleation and mobility at higher temperatures owing to the increased thermal fluctuations assisting in overcoming the activation energy barriers. In fact, at higher temperatures, dislocations loops are seen to have higher mobility and glide further into the substrate. A few small-sized ISFs are observed to form around the indentation pit at 10 K, attributable to the very limited dissociation of perfect dislocations at low temperatures. Nevertheless, at higher temperatures, perfect dislocations are more prone to dissociation, leading to the successive emission of partial dislocations leaving behind numerous ISFs around the indentation region. An interesting observation is the formation of ISFs, surrounded by Shockley partials, within the prismatic loops which grow as the indentation advances, as shown in Figure 15. This mechanism is observed at temperatures higher than 1000 K in our simulations.

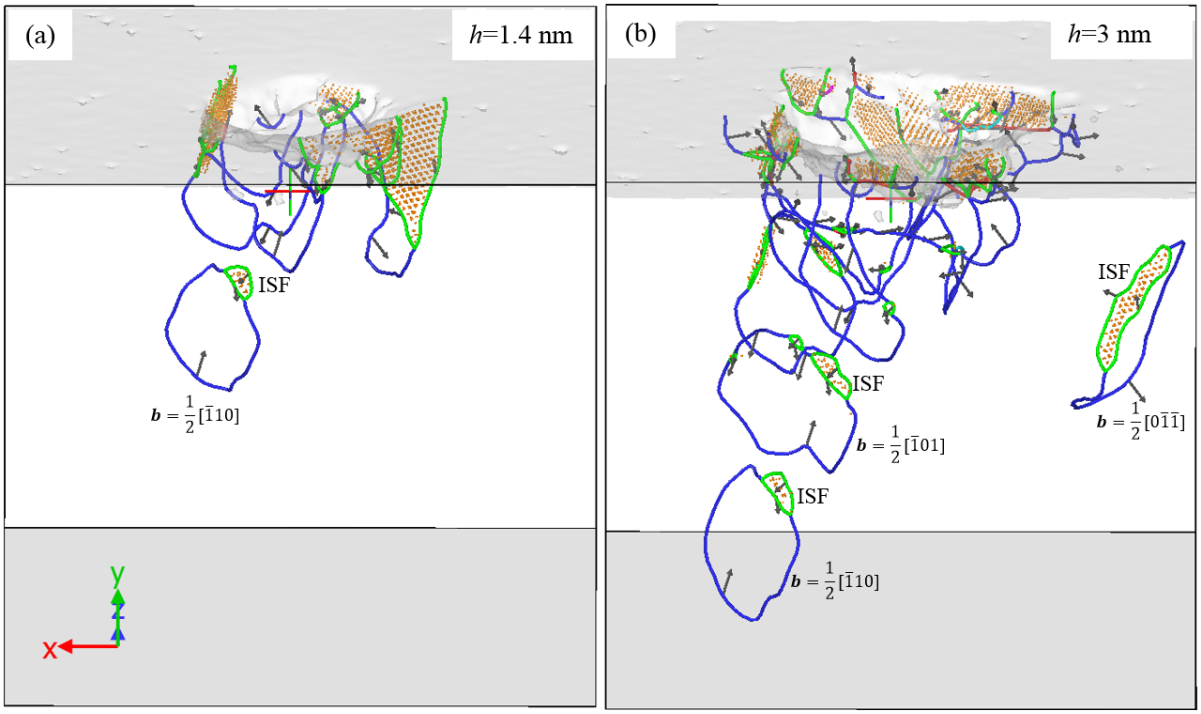

Figure 15 Snapshots showing the formation of ISFs, surrounded by Shockley partials, within the prismatic loops in the twin-free single crystal at T=1000 K.

As shown in Supplementary Movie 5, prismatic loops comprising of two or three ISFs are emitted in the nanotwinned single crystalline substrate with λ=12 nm at T=1000 K, which are absorbed by the CTB. Similar nucleation process and formation of prismatic loops and ISFs can be found at T=2000 K. Further analyses show that dislocation-CTB interactions and transmission mechanisms at high temperatures are akin to those of low and room temperatures, i.e. nucleation of twinning partial dislocations and formation and annihilation of point defects at the CTB. More importantly, no direct transmission takes place at high temperatures, suggesting that direct slip transmission mechanism is not temperature-dependent. However, more lattice dislocations are transmitted across the CTB at high temperatures, which is a direct result of more intensive dislocation activity and mobility at high temperatures. In our simulations of nanotwinned single crystalline substrate with λ=12 nm, the density of transmitted full dislocations rises up to approximately twofold while increasing the temperature

from 10 K to 2000 K, e.g., $3.6 \times 10^{15}\ \mathrm{m}^{-2}$ at 10 K to $6.7 \times 10^{15}\ \mathrm{m}^{-2}$ at 2000 K. Supplementary Figure S1 shows the evolution of full dislocation density for the representative cases of twin-free and nanotwinned single crystals with λ=12 nm and λ=3 nm at different temperatures. It can be seen that the influence of CTBs on dislocation density is more pronounced at low temperatures, e.g., 10 K, implying the high effectiveness of CTBs in dislocation blockage at low temperatures. Moreover, although thermally-activated dislocation processes can increase the dislocation density in the substrate, dislocation emission is a mechanically-driven process requiring a minimum critical stress. It appears that at high temperature of 2000 K, this critical value is not achieved primarily due to the thermal softening mechanisms owing to the increased atomic displacements and interatomic distances [25, 26, 76]. Our simulations also indicate that nanoscale twins are stable even at high temperatures and detwinning does not take place. However, as a consequence of the thermally-activated dislocation nucleation processes, more lattice dislocations nucleate and propagate, leading to accumulation of more twinning partials which could affect the coherency of CTBs.

Analysis of density of full dislocations of twin-free and nanotwinned nanocrystalline samples with *d*=8 nm and λ=3 nm, presented in Supplementary Figure S2, indicates that the density of pre-existing dislocations residing at GBs in the twin-free nanocrystals is generally higher than those of the nanotwinned samples at the same temperature. Furthermore, the density of pre-existing dislocations increases with temperature, except that at the highest temperature of 2000 K plausibly due to the annihilation of dislocations at GBs during dynamic relaxation as a result of the high kinetics of dislocations. Supplementary Figure S3 demonstrates that some pre-existing dislocations located around the indentation region slightly grow and propagate, with a few dislocations emitted from the indentation surface. Thus, as discussed in Section 3.2, intergranular mechanisms along with some limited intragranular deformation mechanisms govern the plastic deformation of twin-free nanocrystalline sample with *d*=8 nm at low and

high temperatures. Note that at high temperatures of 1000 K and 2000 K, a few ISFs are formed in the grain in the twin-free samples, which may improve their plasticity. In the case of the nanotwinned samples, CTBs also cooperate to accommodate the plastic strain at different temperatures.

Indentation speed. To examine the effects of indentation speed, nanotwinned single crystals and nanocrystalline samples with d=8 nm and λ=3 nm, T=300 K and R=6 nm are selected. The indentation speed varies from 5 to 100 m/s. As shown in Supplementary Figure S4, at low indentation speeds, e.g., 5 and 10 m/s, nucleation and propagation of lattice dislocations in the nanotwinned single crystals are more homogenous than those of higher indentation speeds. The dislocation density increases with increasing indentation speed, as a result of a higher dislocation mobility. Nucleation of Shockley partials at the early defect-nucleation stage is seen to be more prevalent at lower indentation speeds. A detailed analysis of the evolving dislocation structure under the indenter uncovers that the onset of plastic deformation is delayed at higher indentation speeds, e.g., the initial nucleation of lattice dislocations occurs at h~1.29 nm at the indentation speed of 5 m/s, whereas it transpires at h~1.39 nm for 100 m/s. It is also found that the dislocation transmission mechanisms across the CTB is independent of the indentation speed.

Supplementary Figure S4 also illustrates the density of full dislocations and defect structure of the nanotwinned nanocrystalline sample with d=8 nm and λ=3 nm obtained at different indentation speeds. Due to the activity of pre-existing dislocations at GBs and stochastic nature of lattice dislocation nucleation, no specific trend correlating the indentation speed and the dislocation density can be found. The full dislocation density varies between 1.3×10^{16} m^{-2} and 1.9×10^{16} m^{-2} for the studied indentation speeds. The variation of the dislocation density during indentation is found to be the lowest at the high indentation speed of 100 m/s, which is of the order of 3.2×10^{15} m^{-2}. A close look at the dislocation nucleation process around the

indentation pit shown in Supplementary Figure S4g-n indicates that the slip activity is very limited for all the studies cases, however, it is marginally higher at the lower speeds. It can therefore be inferred that GB and CTB accommodation processes along with low dislocation activity mainly control the plasticity at low indentation speeds up to 50 m/s, however, at higher speeds, i.e. 100 m/s, the contribution of GB sliding and CTB migration is more pronounced.

3.4. Nanoindentation hardness of single and nanocrystalline samples

To determine the overall response of nanotwinned single crystals, the indentation load-displacement curve is plotted and the average hardness H is calculated over the 3-6 nm indentation depth, where the dislocation-CTB interaction has already occurred in the substrates, and the values of H have reached a steady state. Figure 16a shows the indentation load-displacement curves of the twin-free and nanotwinned single crystalline samples, where there exist numerous drops or fluctuations associated with various plastic deformation mechanisms. As shown in Figure 16b, the "pop-in" event for the twin-free and nanotwinned single crystals is seen at h~1.3 nm, corresponding to the initiation of dislocation activity. However, there is a slight effect of the CTB density on the pop-in load, i.e. high CTB density samples with λ=3 nm and λ=1.5 nm, have lower pop-in load up to ~4.3% than that of the twin-free substrate, implying a reduced elastic deformation stage. This observation suggests that the high density of CTBs may marginally decrease the minimum critical stress for the incipient of plasticity. Figure 16b also indicates that all the curves are overlapped in the elastic regime except for the high CTB density sample with λ=1.5 nm, pointing out to the fact that very high density of CTB may lower the Young's modulus of the nanostructured ceramic materials.

The indentation hardness-displacement curves and the averaged hardness with respect to λ are given in Figure 16a and Figure 16c, respectively. The average hardness of the nanotwinned single crystals is up to ~2.6% higher than that of their twin-free counterpart, which can be

attributed to the dislocation blockage effects of the nanotwins. In addition, the indentation hardness exhibits a clear dependence on the underlying CTB density. On the other hand, CTBs can impose both strengthening and softening effects. We interpret this distinct behaviour as: dislocation blockage for the low CTB density, e.g. nanotwinned sample with λ=12 nm, can impose strengthening effect, leading to the increase of hardness, yet in the nanotwinned substrate with λ=8 nm, a higher density of dislocations at the first CTB culminates in a highly-defective CTB which in turn reduces its dislocation blockage effect. As for the nanotwinned 3C-SiC substrate with λ=6 nm, the first nanoscale twin under the indenter is destroyed by the indenter leading to further softening. Nevertheless, when λ is further decreased, the indenter is almost always in contact or very close to a CTB and so the blockage effect exists persistently, which can compensate the softening effects arising from defective and destroyed CTBs. By and large, a complex interplay among CTB-induced dislocation blockage and softening effects of defective and destroyed CTBs determine the strength of the nanotwinned 3C-SiC subjected to nanoindentation loading. It can be deduced from the above discussion that to benefit the strengthening effects of nanoscale twins in the single crystalline 3C-SiC ceramic subjected to nanoindentation loading, the location of first CTB should be optimally chosen. In the future, we will explore samples with non-uniformly distributed CTBs to specifically quantify the influence of the first CTB location on the nanomechanical response of 3C-SiC ceramic.

It should be mentioned that the room temperature indentation hardness of single crystal 3C-SiC (100) tested by Berkovich indenter with the radius of ~100 nm, as grown by a hot-wall chemical vapor deposition (CVD) process, is 31.2 ± 3.7 GPa [77]. Considering the indentation size effects, indentation speed, morphology of the substrate, higher hardness on the (111) orientation than (110) and (001) [78], the indentation hardness of twin-free single crystal 3C-SiC obtained in our simulations, i.e. ~38.6 GPa, is in agreement with the experiment.

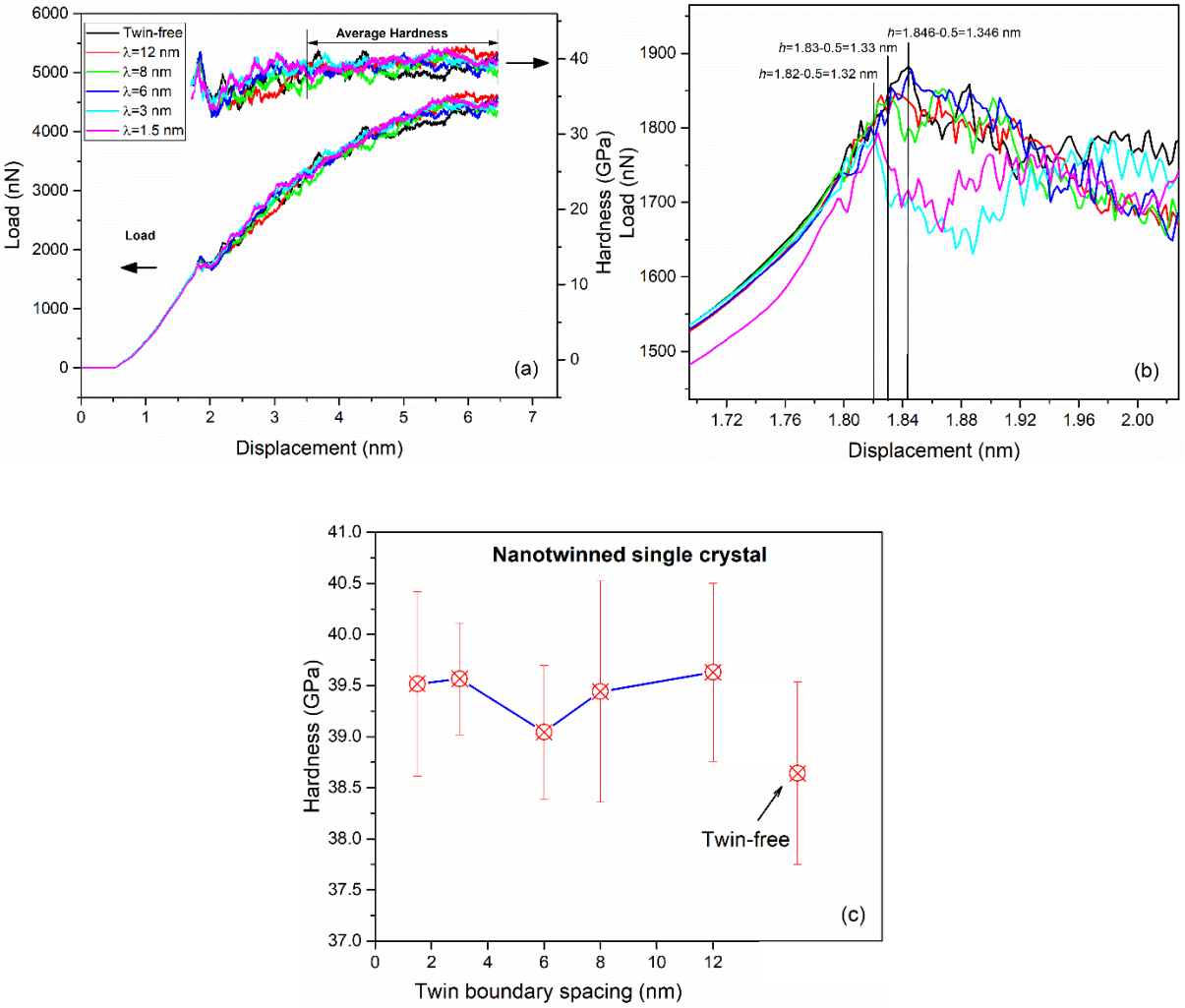

Figure 16 (a) Indentation load-displacement and hardness-displacement curves of the twin-free and nanotwinned single crystal samples, (b) Zoomed view of the load-displacement where pop-in occurs, (c) variation of average indentation hardness with λ. The error bars represent standard deviation.

The resulting average values of the indentation hardness for the twin-free nanocrystalline 3C-SiC are presented in Figure 17. Clearly, nanocrystals have lower indentation hardness compared to the single crystal, and the hardness decreases monotonically with the decrease of the grain size, signifying that GBs under indentation induce a pronounced softening effect, known as the inverse Hall-Petch effect. A feasible physical explanation for this trend would be the decrease of the volume fraction of crystalline phase as well as the increased portion of the GB-mediated deformation mechanisms in the substrates, as discussed in Section 3.2. Our

results agree with the MD observations of Szlufarska and colleagues [32], who found that single crystalline 3C-SiC exhibited a higher scratch hardness compared to the nanocrystalline sample with *d*=5 nm, which was explained by the additional deformation mechanisms via GB sliding in the nanocrystal. Higher indentation hardness of single crystals compared to nanocrystalline counterparts has also been reported in atomistic simulations of Ni [79], Cu [80] and Au [81]. Lower shear strength of nanotwinned $B_{13}C_2$ [20] and B_6O [21] ceramics compared to the perfect structure has been observed. It should be noted the indentation hardness of CVDed polycrsytalline 3C-SiC under a C_3H_8 atmosphere is 33.5 ± 3.3 GPa [77], and that of the pulsed laser deposited (PLD) nanocrystalline SiC films under a CH_4 atmosphere is 32.6-37.3 GPa [82]. On the other hand, the microhardness of polycrystalline 3C-SiC, grown by activated reactive evaporation, is 17.2-36.1 GPa [83]. It is inferred that a wide range of hardness has been reported [77, 82, 83] for the poly/nanocrystalline 3C-SiC, attributable to the morphology of the samples. Experimental studies show that, aside from the crystalline fraction of nanocrystalline 3C-SiC, the composition of the disordered phase residing in GBs plays a crucial role in determining the hardness of the 3C-SiC films. For instance, higher level of hydrogen content in the disordered phase of nanocrystalline 3C-SiC film, deposited on molybdenum by the thermal plasma CVD technique, improves the hardness [84]. The question then arises as to how composition of the disordered phase and hydrogen content can enhance the hardness of 3C-SiC film. This issue poses further endeavors which can be pursued using atomistic simulations. Also, recent TEM analysis of superhard SiC films ($H > 40\text{GPa}$), deposited on silicon by unbalanced magnetron sputtering technique, indicates that a nanocomposite structure composed of crystalline nanocolumnar grains dispersed in an amorphous SiC matrix is the key factor giving rise to the superhardness. To obtain such nanocomposite structure, ion bombardment on the film surface during the deposition is required

[85]. A comprehensive atomistic-based modeling study describing these nanoscale phenomena remains an open and promising research avenue.

To elucidate the effect of CTBs on the indentation hardness of nanocrystalline 3C-SiC samples, the average hardness values are extracted from hardness-displacement curves and are shown in Figure 17. The graphs suggest that the CTBs within nanocrystalline 3C-SiC can have a substantial influence on the indentation hardness behavior arising from the change in the activated deformation mechanisms. Nanotwinned nanocrystals with d=15 and d=8 nm have lower indentation hardness, up to ~6.8% and 2.2%, respectively, than the twin-free counterpart. In contrast, twining can slightly increase the indentation hardness, up to ~0.7%, of 4 nm grain size nanocrystal. We remark that while with large error bars, the average reported trend is correct. However, no specific trend can be detected to generalize the effect of CTB density on the nanocrystalline 3C-SiC. It can be assumed that in the nanocrystals with $d \geq 8$ nm, CTB planes can carry plastic strain, as shown in Figure 13, which may impose softening. However, it is not possible to extend this postulation to the nanocrystals with d=4 nm, where high volume fraction of GBs exists and intergranular deformation mechanisms mainly control the plasticity. However, it is likely that high density of CTBs in small grains limits GB migration and contributes further to the strengthening. Another possible explanation of the observed stochastic trend in the indentation hardness of nanotwinned nanocrystalline materials is that in each sample, the grains directly lying under the indenter could have different crystal orientations, leading to the slightly different hardness values. However, it was found that the indentation location, i.e. where the indenter is first applied at the beginning of indentation, e.g., GB or grain interior, does not contribute to the overall stochastic behavior of hardness observed in our simulations.

It is realized that the nanotwinned nanocrystals with d=15 nm and d=4 nm share some common features in the variation of hardness with λ, e.g., indentation hardness decrease with increasing

λ up to λ=3. In fact, minimum hardness value is obtained at λ=3 nm for both cases. In the nanotwinned nanocrystals with *d*=8 nm, the hardness increases with the decrease of λ up to λ =3 nm, although, as mentioned above, the hardness values are lower than that of the twin-free counterpart. These findings suggest that the indentation hardness in the nanotwinned nanocrystalline 3C-SiC is characterized by a complex combination of grain size, crystalline fraction, density of CTB, dislocation activity, crystallographic orientation of grains located directly beneath the indenter.

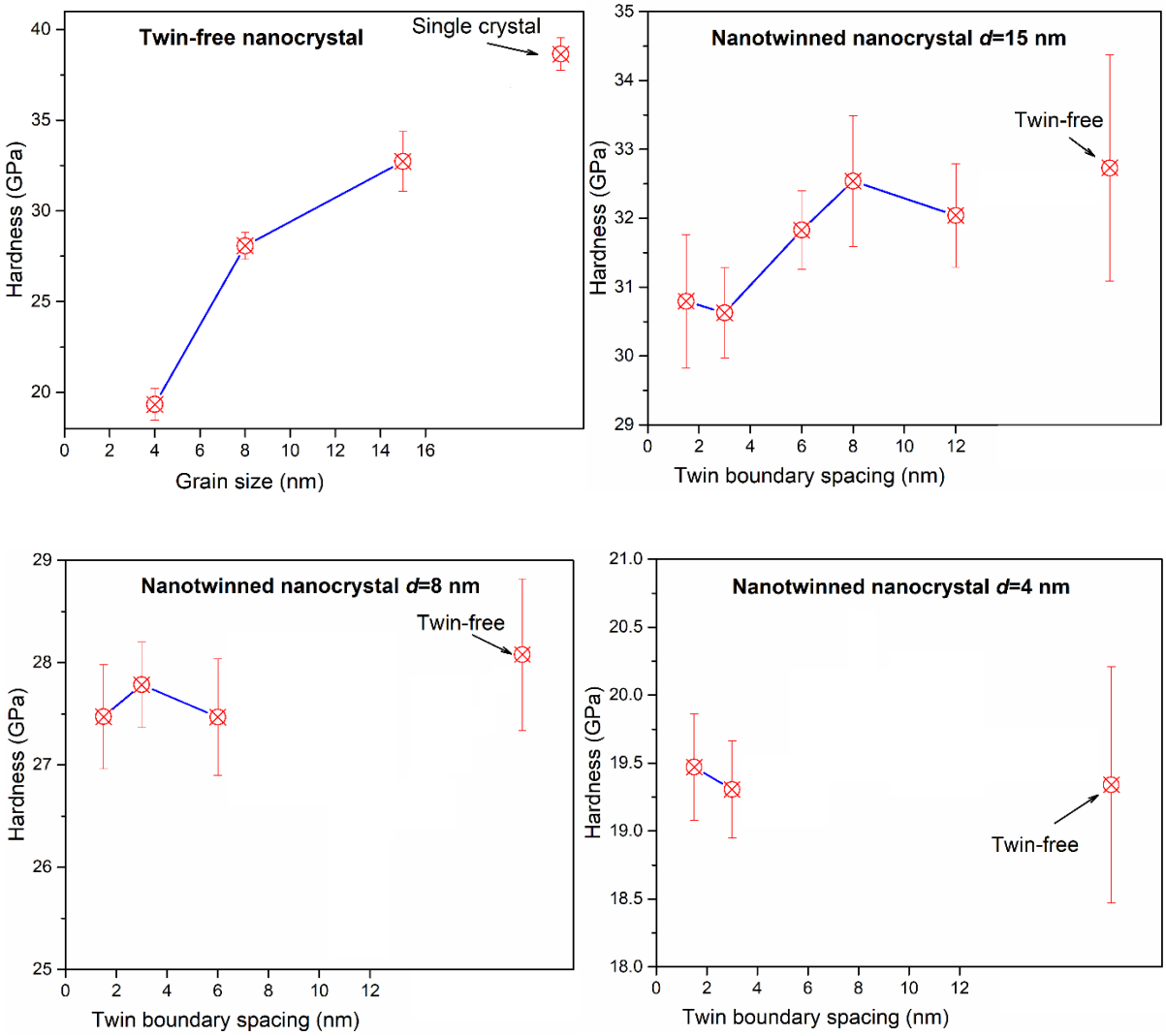

Figure 17 Variation of hardness of twin-free and nanotwinned nanocrystalline samples with grain size and CTB spacing.

To determine the influence of temperature, indentation speed, and indenter size on the hardness of nanotwinned 3C-SiC samples, the nanotwinned single crystal sample with $\lambda = 3$ nm and the nanocrystalline substrate with d=8 nm are selected as the representative cases. Figure 18 shows the variation of indentation hardness with temperature, where the hardness decreases linearly with the increasing temperature, attributable to the thermally-activated and softening mechanisms described in Section 3.3. The indentation hardness of the nanotwinned single and nanocrystalline samples, respectively, is found to decrease by ~88% and ~97% when the temperature increases from 10 to 2000 K, suggesting that the temperature effects are more pronounced for the nanotwinned nanocrystalline samples. As Figure 18 demonstrates, the indentation hardness increases with the indentation speed, however, a slight decrease can be seen for the nanotwinned nanocrystalline sample while increasing the indentation speed from 50 to 100 m/s, which may be attributed to the improved GB sliding at high indentation speeds. As expected, increasing temperature or decreasing the indentation speed lowers the onset of plasticity of the nanotwinned single crystals, i.e. pop-in load reduces by ~29% and ~32% when decreasing the indentation speed from 100 to 5 m/s or increasing the temperature from 10 to 600 K, respectively. Note that at higher temperatures the pop-in event was not detectable due to the intensified waviness of the load-displacement curve caused by the enhanced kinetics. Also, in nanocrystals, a smooth transition from elastic to plastic deformation takes place in the simulations thus pop-in excursion was absent on the load-displacement graphs. Figure 18e shows a decreasing hardness with increasing indenter radius, confirming the indentation size effect (ISE) for spherical indentation [86]. This reduction is linear for the nanotwinned single crystalline sample whereas in the nanocrystalline counterpart the hardness first decreases marginally then experiences a sharp drop. It can be assumed that increasing indenter size greater than the mean grain size of the sample would culminate in shifting the deformation

mechanisms from intragranular to intergranular plasticity, e.g., enhanced GB sliding, leading to the improved plasticity. Such effect can be perceived when using the indenter with R=8 nm. The indentation hardness of the nanotwinned single and nanocrystalline samples, respectively, decreases by ~9.5% and ~17.5% when the indenter radius increases from 4 to 8 nm, indicative of higher ISE in the nanocrystals. By comparing the hardness results, it is inferred that nanocrystalline samples are more affected by the test conditions.

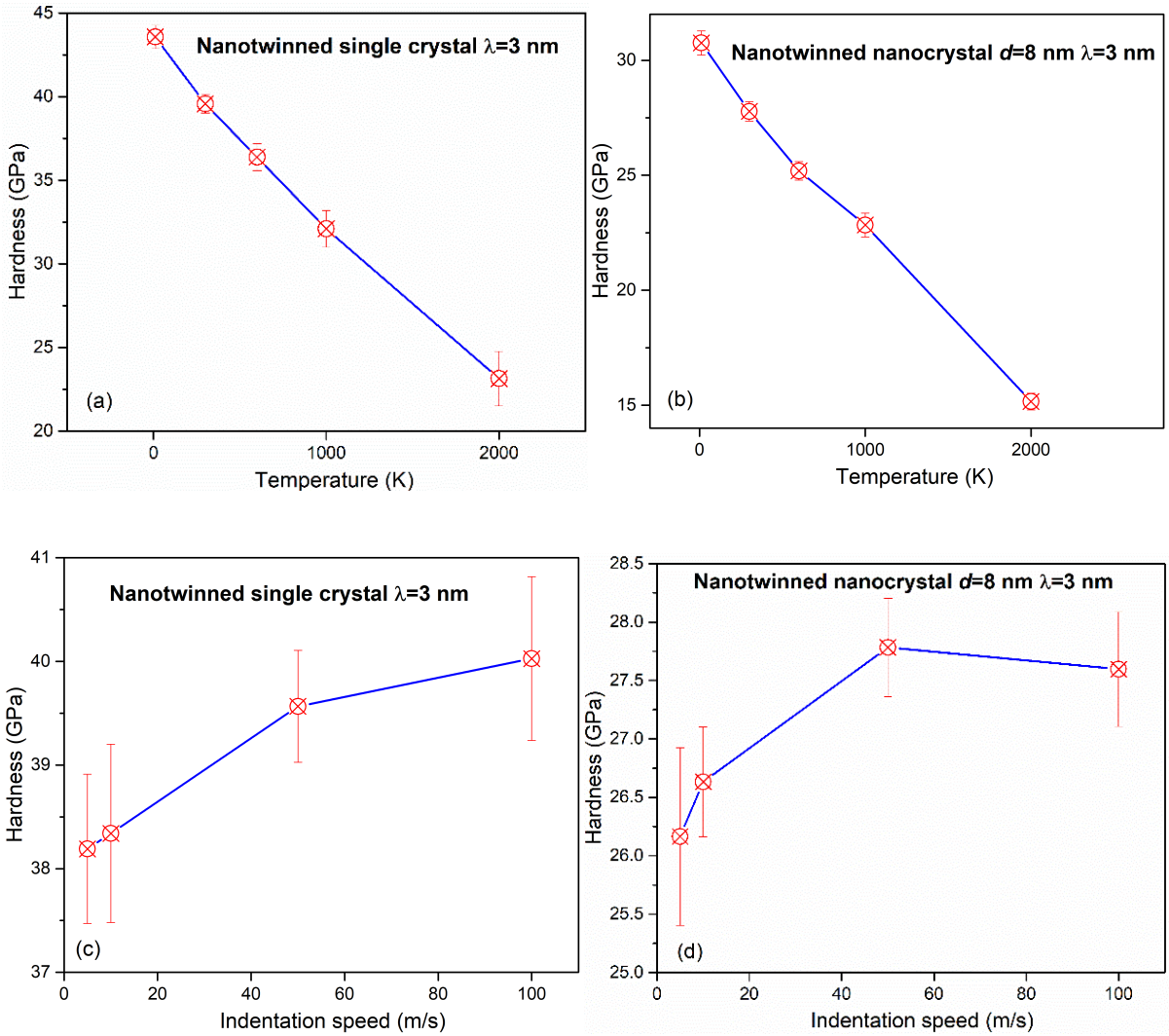

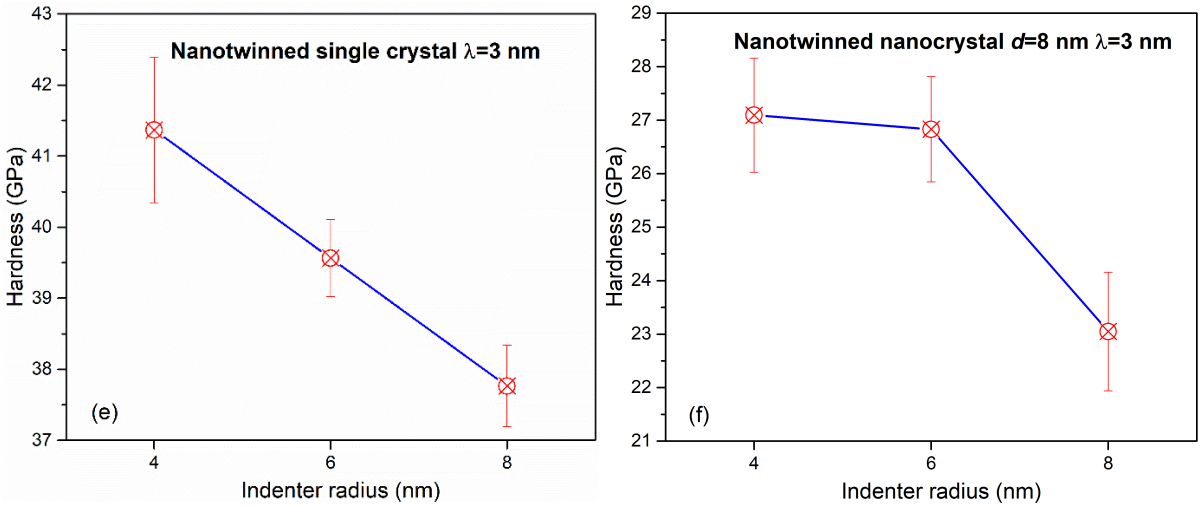

Figure 18 Effect of (a-b) temperature, (c-d) indentation speed, and (e-f) indenter size on the hardness of nanotwinned single crystalline and nanocrystalline samples.

4. Conclusions

In the present work, large-scale MD simulations were implemented to characterize deformation mechanisms and nanomechanical responses of twin-free and nanotwinned single/nanocrystalline 3C-SiC ceramic subjected to nanoindentation loading. Key conclusions are as follows:

1- Mechanisms responsible for the lattice dislocation transmission include nucleation of twinning partial dislocations and formation and annihilation of point defects at CTBs, which are independent of certain parameters such as temperature, indentation speed, and indenter size. The presence of a high CTB density triggers the twinning dislocation mechanism to shift from dissociation and propagation of Frank-type sessile partials to Shockley partials forming half-loops within the CTB.

2- In highly twinned nanocrystalline nanostructures with a large enough grain (of the order of 8 nm), CTBs can accommodate a fraction of imposed shear strain thus contributing to the plasticity; however, in substrates with small grains, CTBs and lattice dislocations have trivial influence on the deformation plasticity.

3- “Lasso”-like mechanism of prismatic loop formation via intersection and annihilation of screw dislocations is associated with the augmented dislocation nucleation and mobility at higher temperatures. High temperature also prompts formation of ISFs within prismatic loops in the twin-free and nanotwinned single crystals. The influence of CTBs on dislocation density is found to be more pronounced at low temperatures, implying the effectiveness of CTBs in dislocation blockage at low temperatures.

4- GB and CTB accommodation processes along with low dislocation activity mainly control the plasticity at low indentation speeds; however, at higher speeds, the contributions by GB sliding and CTB migration are more pronounced.

5- Twining can improve the indentation resistance of the single crystalline substrate, however, the indentation hardness exhibits a clear dependence on the underlying CTB density. In particular, as most lattice dislocations accumulate at the first CTB under the indenter, the location of the first CTB plays a key role in strengthening the substrate. Compared to the single crystal, nanocrystals have lower indentation hardness, which decreases monotonically with the decrease of grain size, signifying that GBs under indentation induce a pronounced softening effect owing to the increased fraction of disordered intergranular phases and enhanced GB-based deformation processes.

6- Twining can slightly increase the indentation hardness of small grain size, of the order of 4 nm, nanotwinned nanocrystals, however, shows a reverse Hall-Petch-like effect for large grain size nanocrystals. No specific trend is observed to generalize the effect of the CTB density on the nanocrystalline substrates. Moreover, for the same CTB spacing, the indentation hardness of nanocrystalline samples are more affected by the test conditions than the single crystals.

Acknowledgements

SZC would like to express his sincere gratitude for the financial support from the BIAM-Imperial Centre for Materials Characterisation, Processing and Modelling at Imperial College London. SZC also acknowledges the use of High Performance Computing (HPC) facilities at Imperial College London. The work of SX was supported in part by the Elings Prize Fellowship in Science offered by the California NanoSystems Institute (CNSI) on the UC Santa Barbara campus. SX also acknowledges support from the Center for Scientific Computing from the CNSI, MRL: an NSF MRSEC (DMR-1121053). This work used the Extreme Science and Engineering Discovery Environment (XSEDE), which is supported by National Science Foundation grant number ACI-1053575.

References

1. I.J. Beyerlein, X. Zhang, and A. Misra: Growth twins and deformation twins in metals. Annual Review of Materials Research. **44**, 329-363 (2014).
2. E. Hall: The deformation and ageing of mild steel: III discussion of results. Proceedings of the Physical Society. Section B. **64**, 747 (1951).
3. N. Petch: The Cleavage Strengh of Polycrystals. J. of the Iron and Steel Inst. **174**, 25-28 (1953).
4. S. Xu, L. Xiong, Y. Chen, and D.L. McDowell: Sequential slip transfer of mixed-character dislocations across Σ3 coherent twin boundary in FCC metals: a concurrent atomistic-continuum study. npj Computational Materials. **2**, 15016 (2016).
5. S. Xu, L. Xiong, Y. Chen, and D.L. McDowell: Comparing EAM potentials to model slip transfer of sequential mixed character dislocations across two symmetric tilt grain boundaries in Ni. JOM. **69**, 814-821 (2017).
6. X. Li, Y. Wei, L. Lu, K. Lu, and H. Gao: Dislocation nucleation governed softening and maximum strength in nano-twinned metals. Nature. **464**, 877 (2010).
7. L. Lu, X. Chen, X. Huang, and K. Lu: Revealing the maximum strength in nanotwinned copper. Science. **323**, 607-610 (2009).
8. A. Stukowski, K. Albe, and D. Farkas: Nanotwinned fcc metals: Strengthening versus softening mechanisms. Physical Review B. **82**, 224103 (2010).
9. S. Xu, J.K. Startt, T.G. Payne, C.S. Deo, and D.L. McDowell: Size-dependent plastic deformation of twinned nanopillars in body-centered cubic tungsten. Journal of Applied Physics. **121**, 175101 (2017).
10. S. Xu and S.Z. Chavoshi: Uniaxial deformation of nanotwinned nanotubes in body-centered cubic tungsten. Current Applied Physics. **18**, 114-121 (2018).
11. S. Xu, S.Z. Chavoshi, and Y. Su: Deformation Mechanisms in Nanotwinned Tungsten Nanopillars: Effects of Coherent Twin Boundary Spacing. physica status solidi (RRL)-Rapid Research Letters. (2018).
12. T. Zhu and H. Gao: Plastic deformation mechanism in nanotwinned metals: an insight from molecular dynamics and mechanistic modeling. Scripta Materialia. **66**, 843-848 (2012).
13. X. Li, S. Yin, S.H. Oh, and H. Gao: Hardening and toughening mechanisms in nanotwinned ceramics. Scripta Materialia. **133**, 105-112 (2017).

14. Q. Huang, D. Yu, B. Xu, W. Hu, Y. Ma, Y. Wang, Z. Zhao, B. Wen, J. He, and Z. Liu: Nanotwinned diamond with unprecedented hardness and stability. Nature. **510**, 250 (2014).
15. C. Huang, X. Peng, B. Yang, Y. Zhao, H. Xiang, X. Chen, Q. Li, and T. Fu: Molecular dynamics simulations for responses of nanotwinned diamond films under nanoindentation. Ceramics International. (2017).
16. Y. Tian, B. Xu, D. Yu, Y. Ma, Y. Wang, Y. Jiang, W. Hu, C. Tang, Y. Gao, and K. Luo: Ultrahard nanotwinned cubic boron nitride. Nature. **493**, 385-388 (2013).
17. S. Zheng, R. Zhang, R. Huang, T. Taniguchi, X. Ma, Y. Ikuhara, and I.J. Beyerlein: Structure and energetics of nanotwins in cubic boron nitrides. Applied Physics Letters. **109**, 081901 (2016).
18. Q. An, W.A. Goddard III, K.Y. Xie, G.-d. Sim, K.J. Hemker, T. Munhollon, M.F. Toksoy, and R.A. Haber: Superstrength through Nanotwinning. Nano letters. **16**, 7573-7579 (2016).
19. K.Y. Xie, Q. An, M.F. Toksoy, J.W. McCauley, R.A. Haber, W.A. Goddard III, and K.J. Hemker: Atomic-level understanding of "asymmetric twins" in boron carbide. Physical review letters. **115**, 175501 (2015).
20. Q. An and W.A. Goddard III: Nanotwins soften boron-rich boron carbide (B13C2). Applied Physics Letters. **110**, 111902 (2017).
21. Q. An, K.M. Reddy, J. Qian, K.J. Hemker, M.-W. Chen, and W.A. Goddard Iii: Nucleation of amorphous shear bands at nanotwins in boron suboxide. Nature communications. **7**, (2016).
22. Q. An, K.M. Reddy, H. Dong, M.-W. Chen, A.R. Oganov, and W.A. Goddard III: Nanotwinned Boron Suboxide (B6O): New Ground State of B6O. Nano letters. **16**, 4236-4242 (2016).
23. S.Z. Chavoshi and X. Luo: Atomic-scale characterization of occurring phenomena during hot nanometric cutting of single crystal 3C–SiC. RSC Advances. **6**, 71409-71424 (2016).
24. S.Z. Chavoshi, S.C. Gallo, H. Dong, and X. Luo: High temperature nanoscratching of single crystal silicon under reduced oxygen condition. Materials Science and Engineering: A. **684**, 385-393 (2017).
25. S.Z. Chavoshi, S. Goel, and X. Luo: Molecular dynamics simulation investigation on the plastic flow behaviour of silicon during nanometric cutting. Modelling and Simulation in Materials Science and Engineering. **24**, 015002 (2015).
26. S.Z. Chavoshi and X. Luo: An atomistic simulation investigation on chip related phenomena in nanometric cutting of single crystal silicon at elevated temperatures. Computational Materials Science. **113**, 1-10 (2016).
27. S.Z. Chavoshi, S. Xu, and X. Luo: Dislocation-mediated plasticity in silicon during nanometric cutting: A molecular dynamics simulation study. Materials Science in Semiconductor Processing. **51**, 60-70 (2016).
28. S.Z. Chavoshi and X. Luo: Molecular dynamics simulation study of deformation mechanisms in 3C–SiC during nanometric cutting at elevated temperatures. Materials Science and Engineering: A. **654**, 400-417 (2016).
29. Z. Lin, L. Wang, J. Zhang, X.-Y. Guo, W. Yang, H.-K. Mao, and Y. Zhao: Nanoscale twinning-induced elastic strengthening in silicon carbide nanowires. Scripta Materialia. **63**, 981-984 (2010).
30. D.-H. Wang, D. Xu, Q. Wang, Y.-J. Hao, G.-Q. Jin, X.-Y. Guo, and K. Tu: Periodically twinned SiC nanowires. Nanotechnology. **19**, 215602 (2008).
31. Z. Wang, J. Li, F. Gao, and W.J. Weber: Tensile and compressive mechanical behavior of twinned silicon carbide nanowires. Acta Materialia. **58**, 1963-1971 (2010).
32. M. Mishra, C. Tangpatjaroen, and I. Szlufarska: Plasticity‐Controlled Friction and Wear in Nanocrystalline SiC. Journal of the American Ceramic Society. **97**, 1194-1201 (2014).
33. I. Szlufarska, A. Nakano, and P. Vashishta: A crossover in the mechanical response of nanocrystalline ceramics. Science. **309**, 911-914 (2005).
34. Q. Liu, H. Luo, L. Wang, and S. Shen: Tuning the thermal conductivity of silicon carbide by twin boundary: a molecular dynamics study. Journal of Physics D: Applied Physics. **50**, 065108 (2017).

35. H. Wang, W. Zhang, C. Wang, J. Ma, and P. Huai: Molecular dynamics study of thermal transport across grain boundaries in silicon carbide nanorod. Materials Research Express. **3**, 035018 (2016).
36. E. Jin, L.-S. Niu, E. Lin, and Z. Duan: Effects of irradiation on the mechanical behavior of twined SiC nanowires. Journal of Applied Physics. **113**, 104309 (2013).
37. N. Swaminathan, M. Wojdyr, D.D. Morgan, and I. Szlufarska: Radiation interaction with tilt grain boundaries in β-SiC. Journal of Applied Physics. **111**, 054918 (2012).
38. N. Swaminathan, P.J. Kamenski, D. Morgan, and I. Szlufarska: Effects of grain size and grain boundaries on defect production in nanocrystalline 3C–SiC. Acta Materialia. **58**, 2843-2853 (2010).
39. F. Gao, D. Chen, W. Hu, and W.J. Weber: Energy dissipation and defect generation in nanocrystalline silicon carbide. Physical Review B. **81**, 184101 (2010).
40. A. Moriani and F. Cleri: Point-defect recombination efficiency at grain boundaries in irradiated SiC. Physical Review B. **73**, 214113 (2006).
41. D. Chen, F. Gao, and B. Liu: Grain boundary resistance to amorphization of nanocrystalline silicon carbide. Scientific reports. **5**, (2015).
42. C.A. Zorman and R.J. Parro: Micro‐and nanomechanical structures for silicon carbide MEMS and NEMS. physica status solidi (b). **245**, 1404-1424 (2008).
43. S. Z. Chavoshi and S. Xu: Temperature-dependent nanoindentation response of materials. MRS Communications. **8**, 15-28 (2018).
44. S.Z. Chavoshi and S. Xu: A review on micro-and nanoscratching/tribology at high temperatures: instrumentation and experimentation. Journal of Materials Engineering and Performance. **27**, 3844-3858 (2018).
45. S. Plimpton: Fast parallel algorithms for short-range molecular dynamics. Journal of computational physics. **117**, 1-19 (1995).
46. P. Vashishta, R.K. Kalia, A. Nakano, and J.P. Rino: Interaction potential for silicon carbide: a molecular dynamics study of elastic constants and vibrational density of states for crystalline and amorphous silicon carbide. Journal of applied physics. **101**, 103515-103528 (2007).
47. S.Z. Chavoshi and S. Xu: Nanoindentation/scratching at finite temperatures: Insights from atomistic-based modeling. Progress in Materials Science. **In Press**, (2018).
48. S.Z. Chavoshi, S. Xu, and S. Goel: Addressing the discrepancy of finding the equilibrium melting point of silicon using molecular dynamics simulations. Proc. R. Soc. A. **473**, 20170084 (2017).
49. S. Xu, Y. Su, and S.Z. Chavoshi: Deformation of periodic nanovoid structures in Mg single crystals. Materials Research Express. **5**, 016523 (2018).
50. F.H. Stillinger and T.A. Weber: Computer simulation of local order in condensed phases of silicon. Physical review B. **31**, 5262 (1985).
51. R. Smith, D. Christopher, S.D. Kenny, A. Richter, and B. Wolf: Defect generation and pileup of atoms during nanoindentation of Fe single crystals. Physical Review B. **67**, 245405 (2003).
52. T. Remington, C. Ruestes, E. Bringa, B. Remington, C. Lu, B. Kad, and M. Meyers: Plastic deformation in nanoindentation of tantalum: A new mechanism for prismatic loop formation. Acta Materialia. **78**, 378-393 (2014).
53. C.L. Kelchner, S. Plimpton, and J. Hamilton: Dislocation nucleation and defect structure during surface indentation. Physical review B. **58**, 11085 (1998).
54. G. Ziegenhain, A. Hartmaier, and H.M. Urbassek: Pair vs many-body potentials: Influence on elastic and plastic behavior in nanoindentation of fcc metals. Journal of the Mechanics and Physics of Solids. **57**, 1514-1526 (2009).
55. G. Ziegenhain, H.M. Urbassek, and A. Hartmaier: Influence of crystal anisotropy on elastic deformation and onset of plasticity in nanoindentation: a simulational study. Journal of Applied Physics. **107**, 061807 (2010).
56. S. Z. Chavoshi and S. Xu: Tension-compression asymmetry in plasticity of nanotwinned 3C-SiC nanocrystals. Journal of Applied Physics. **10.1063/1.5046949**, (2018).

57. A. Stukowski: Visualization and analysis of atomistic simulation data with OVITO–the Open Visualization Tool. Modelling and Simulation in Materials Science and Engineering. **18**, 015012 (2009).
58. A. Stukowski and K. Albe: Extracting dislocations and non-dislocation crystal defects from atomistic simulation data. Modelling and Simulation in Materials Science and Engineering. **18**, 085001 (2010).
59. T. Fu, X. Peng, X. Chen, S. Weng, N. Hu, Q. Li, and Z. Wang: Molecular dynamics simulation of nanoindentation on Cu/Ni nanotwinned multilayer films using a spherical indenter. Scientific reports. **6**, (2016).
60. S. Sun, X. Peng, H. Xiang, C. Huang, B. Yang, F. Gao, and T. Fu: Molecular dynamics simulation in single crystal 3C-SiC under nanoindentation: Formation of prismatic loops. Ceramics International. **43**, 16313-16318 (2017).
61. H. Xiang, H. Li, T. Fu, C. Huang, and X. Peng: Formation of prismatic loops in AlN and GaN under nanoindentation. Acta Materialia. **138**, 131-139 (2017).
62. I.A. Alhafez, C.J. Ruestes, Y. Gao, and H.M. Urbassek: Nanoindentation of hcp metals: a comparative simulation study of the evolution of dislocation networks. Nanotechnology. **27**, 045706 (2015).
63. Z.-H. Jin, P. Gumbsch, E. Ma, K. Albe, K. Lu, H. Hahn, and H. Gleiter: The interaction mechanism of screw dislocations with coherent twin boundaries in different face-centred cubic metals. Scripta Materialia. **54**, 1163-1168 (2006).
64. N. Li, J. Wang, A. Misra, X. Zhang, J. Huang, and J. Hirth: Twinning dislocation multiplication at a coherent twin boundary. Acta Materialia. **59**, 5989-5996 (2011).
65. Y. Wang, M. Sui, and E. Ma: In situ observation of twin boundary migration in copper with nanoscale twins during tensile deformation. Philosophical Magazine Letters. **87**, 935-942 (2007).
66. T. Zhu, J. Li, A. Samanta, H.G. Kim, and S. Suresh: Interfacial plasticity governs strain rate sensitivity and ductility in nanostructured metals. Proceedings of the National Academy of Sciences. **104**, 3031-3036 (2007).
67. N. Gunkelmann, E.M. Bringa, K. Kang, G.J. Ackland, C.J. Ruestes, and H.M. Urbassek: Polycrystalline iron under compression: Plasticity and phase transitions. Physical Review B. **86**, 144111 (2012).
68. T.J. Rupert and C.A. Schuh: Mechanically driven grain boundary relaxation: a mechanism for cyclic hardening in nanocrystalline Ni. Philosophical Magazine Letters. **92**, 20-28 (2012).
69. J.-H. Ree: Grain boundary sliding and development of grain boundary openings in experimentally deformed octachloropropane. Journal of Structural Geology. **16**, 403-418 (1994).
70. F. Shimizu, S. Ogata, and J. Li: Theory of shear banding in metallic glasses and molecular dynamics calculations. Materials transactions. **48**, 2923-2927 (2007).
71. E.N. Hahn and M.A. Meyers: Grain-size dependent mechanical behavior of nanocrystalline metals. Materials Science and Engineering: A. **646**, 101-134 (2015).
72. G.J. Tucker and S.M. Foiles: Quantifying the influence of twin boundaries on the deformation of nanocrystalline copper using atomistic simulations. International Journal of Plasticity. **65**, 191-205 (2015).
73. H. Van Swygenhoven, D. Farkas, and A. Caro: Grain-boundary structures in polycrystalline metals at the nanoscale. Physical Review B. **62**, 831 (2000).
74. H. Van Swygenhoven, M. Spaczer, and A. Caro: Microscopic description of plasticity in computer generated metallic nanophase samples: a comparison between Cu and Ni. Acta Materialia. **47**, 3117-3126 (1999).
75. J. Knap and M. Ortiz: Effect of indenter-radius size on Au (001) nanoindentation. Physical Review Letters. **90**, 226102 (2003).

76. S.Z. Chavoshi, S. Goel, and X. Luo: Influence of temperature on the anisotropic cutting behaviour of single crystal silicon: A molecular dynamics simulation investigation. Journal of Manufacturing Processes. **23**, 201-210 (2016).
77. J.D. Reddy, A.A. Volinsky, C.L. Frewin, C. Locke, and S.E. Saddow: Mechanical properties of 3C-SiC films for MEMS applications. MRS Online Proceedings Library Archive. **1049**, (2007).
78. H.-P. Chen, R.K. Kalia, A. Nakano, P. Vashishta, and I. Szlufarska: Multimillion-atom nanoindentation simulation of crystalline silicon carbide: Orientation dependence and anisotropic pileup. Journal of Applied Physics. **102**, 063514 (2007).
79. X. Liu, F. Yuan, and Y. Wei: Grain size effect on the hardness of nanocrystal measured by the nanosize indenter. Applied Surface Science. **279**, 159-166 (2013).
80. X.-L. Ma and W. Yang: Molecular dynamics simulation on burst and arrest of stacking faults in nanocrystalline Cu under nanoindentation. Nanotechnology. **14**, 1208 (2003).
81. D. Feichtinger, P. Derlet, and H. Van Swygenhoven: Atomistic simulations of spherical indentations in nanocrystalline gold. Physical Review B. **67**, 024113 (2003).
82. D. Craciun, G. Socol, D. Cristea, M. Stoicanescu, N. Oláh, K. Balazs, N. Stefan, E. Lambers, and V. Craciun: Mechanical properties of pulsed laser deposited nanocrystalline SiC films. Applied Surface Science. **336**, 391-395 (2015).
83. Y.C. Cha, G. Kim, H.J. Doerr, and R.F. Bunshah: Effects of activated reactive evaporation process parameters on the microhardness of polycrystalline silicon carbide thin films. Thin Solid Films. **253**, 212-217 (1994).
84. F. Liao, S. Girshick, W. Mook, W. Gerberich, and M. Zachariah: Superhard nanocrystalline silicon carbide films. Applied Physics Letters. **86**, 171913 (2005).
85. K.E. Bae, K.W. Chae, J.K. Park, W.S. Lee, and Y.J. Baik: Nanocolumnar Composite Microstructure of Superhard SiC Thin Film Deposited Using Unbalanced Magnetron Sputtering Method. Advanced Engineering Materials. **18**, 1123-1126 (2016).
86. J. Swadener, E. George, and G. Pharr: The correlation of the indentation size effect measured with indenters of various shapes. Journal of the Mechanics and Physics of Solids. **50**, 681-694 (2002).